TECHNISCHE UNIVERSITÄT MÜNCHEN

Lehrstuhl für Biologische Bildgebung

Konstruktion des Kathetersystems für intravaskuläre Hybrid-Bildgebung

Dmitry Bozhko

Vollständiger Abdruck der von der Fakultät für Elektrotechnik und Informationstechnik der Technischen Universität München zur Erlangung des akademischen Grades eines

Doktor-Ingenieurs (Dr. –Ing.)

genehmigten Dissertation.

Vorsitzender: Prof. Dr.-Ing. habil. Dr. h.c. Alexander W. Koch
Prüfer der Dissertation:

1. Prof. Dr. Vasilis Ntziachristos.
2. Prof. Dr. Oliver Hayden.

Die Dissertation wurde am 12.07.2018 bei der Technischen Universität München eingereicht und durch die Fakultät für Elektrotechnik und Informationstechnik am 11.08.2019 angenommen.

Table of Contents

Table of Figures

Table of Tables

List of abbreviations

IVUS	Intravascular ultrasound
OCT	Optical coherence tomography
CAD	Coronary artery disease
NIRF	Near-infrared fluorescence
cNIRF	Corrected near-infrared fluorescence
ICG	Indocyanine green
PET	Positron emission tomography
FDG	Fluorodeoxyglucose
CT	Computed tomography
USPIO	Ultrasmall superparamagnetic iron oxide
NIRS	Near-infrared spectroscopy
IVOA	Intravascular optoacoustic
FLIM	Fluorescence lifetime imaging
TCFA	Thin-cap fibroatheroma
NIR	Near-infrared
RTE	Radiative Transport Equation
MC	Monte Carlo
htc	Hematocrit
PZT	Piezoelectric block
SNR	Signal-to-noise ratio
NA	Numerical aperture
FWHM	Full width at half maximum
OD	Outside diameter
ID	Inside diameter
PBS	Phosphate buffered saline
FDA	Food and drug administration
PECAM-1	Platelet and endothelial cell adhesion molecule 1
OFDI	Optical frequency domain imaging

FM	Fluorescence microscopy
FRI	Reflectance fluorescence imaging
rpm	Rotations per minute
DM	Dichroic mirror
PMT	Photomultiplier tube
FEP	Fluorinated ethylene propylene
LDPE	Low-density polyethylene
ECG	Electrocardiography
WL	White light
FFP	Fresh frozen plasma
LAD	Left anterior descending
OA	Optoacoustic
MSOA	Multispectral optoacoustic

1 Abstract

While current clinical intravascular imaging approaches such as intravascular ultrasound (IVUS) and optical coherence tomography (OCT) provide anatomical insights into plaque and vessel structure, they do not provide adequate specificity to serve as routine clinical predictive approaches. Therefore, combined structural and quantitative molecular imaging has emerged as a strategy to advance diagnostics of coronary artery disease (CAD) and to improve prognosis through early identification of vulnerable lesions and guidance of optimal therapy of atherosclerosis. To facilitate this development, we have developed and validated herein a hybrid intravascular catheter for quantitative molecular fluorescence-ultrasound imaging.

We first built a near-infrared fluorescence (NIRF) catheter for reliable molecular imaging. Resolution and sensitivity of the NIRF system was characterized. Its imaging performance was validated by assessment of endothelial integrity in vessels *ex vivo*. Sensitivity optimization extended detection distance and allowed *ex vivo* imaging of vessels up to 6 mm in diameter, and *in vivo* imaging of vessels up to 4 mm in diameter.

To enable co-registration of morphological and florescence imaging, we integrated a stand-alone NIRF catheter with an ultrasound transducer. A reconstruction algorithm was implemented that precisely aligns NIRF and IVUS

data. Additionally, we developed a novel data-driven correction to account for light absorption related to a random catheter position within a vessel. Thus, quantitative fluorescence readings through blood were enabled for the first time. During this work, we discovered that blood attenuation measurement *ex vivo* overestimates the degree of light attenuation that occurs *in vivo.* As a result, we were able to base our correction algorithm on carefully designed *in vivo* attenuation measurements.

Finally, the resulting corrected NIRF-IVUS (cNIRF-IVUS) system was assessed in various clinically relevant *in vivo* scenarios. We tested its ability to detect *in vivo* accumulation of fluorescence agents indocyanine green (ICG) and Prosense VM110 in vessels of different sizes, including vessels with a metallic stent. Reproducibility and reliability of through-blood imaging was thoroughly evaluated.

The overall findings are anticipated to motivate the development of clinical cNIRF-IVUS systems that will allow early diagnosis of coronary artery diseases (CADs) in patients and will allow quantitative therapy guidance and plaque evaluation. As IVUS is already a standard clinical imaging approach, combining it with complementary fluorescence readings as part of standard intravascular catheterization will greatly expand diagnostic abilities and help explore processes underlying plaque formation and development.

2 Introduction

According to the report of the European Heart Network[1] nearly half of all deaths in the European Union (43% of deaths in woman and 36% of deaths in men) are caused by cardiovascular diseases (CVDs). The majority of these cases arise from atherosclerosis. Despite the extremely high death rate, origins of atherosclerosis are still not fully understood. Therefore, there is an urgent need for new imaging methods that will give insights into the underlying biology of atherosclerotic plaque and lead to prediction of complications[2–4].

Atherosclerosis starts when the endothelium covering of the arterial wall gets damaged. Initially, because of the damage, platelets, cellular debris, calcium, and mostly fatty materials such as cholesterol and triglyceride are deposited in the innermost layer of the artery wall where the atherosclerotic fatty streak forms (**Figure 1**). With time, atherosclerotic plaque, consisting of macrophages, underlying cholesterol crystals, and calcification builds up[5]. Plaque disturbs the blood flow and can result in heart attack, stroke, and other severe clinical events. Usually, plaque progresses slowly during decades and atherosclerosis remains asymptomatic until advanced stage or plaque rupture[6]. As plaque rupture could trigger ischemia of the myocardial muscle and damage, it is important to diagnose and identify vulnerable plaques prior to rupture.

NOMANCLATURE AND MAIN HISTOLOGY

Initial lesion
- histologically "normal"
- macrophage infiltration
- isolated foam cells

Fatty streak
mainly intracellular lipid accumulation

Intermediate lesion
- intracellular lipid accumulation
- small extracellular lipid pools

Atheroma
- intracellular lipid accumulation
- core of extracellular lipid

Fibroatheroma
- single or multiple lipid cores
- fibrotic/calcific layers

Complicated lesion
- surface defect
- hematoma-hemorrhage
- thrombosis

ENDOTHEHELIAL DYSFUNCTION

SEQUENCES IN PROGRESSION OF ATHEROSCLEROSIS

*Image from: Wikipedia: The free encyclopedia.

Figure 1. Formation of atherosclerotic plaque in the artery[7].

Various imaging modalities have been developed for the detection of atherosclerosis. Notably, intravascular ultrasound and optical coherence tomography have become primary diagnostic tools for coronary arterial risk assessment. IVUS technology was clinically tested in 1989[8] and still remains widely common. Ultrasound detection enables physicians to image the entire blood vessel wall (penetration depth up to 30 mm) in the presence of blood and offers pullback speeds up to 1 mm/sec[9]. However, IVUS suffers from relatively low resolution: 70-200 μm in the axial direction and 200-300 μm in the lateral direction. OCT, on the other hand, is based on low-coherence optical interferometry and offers superior resolutions of about 20 μm and pullback

speeds up to 20 mm/sec with improved signal to noise ratio (SNR), but requires blood clearance from the field of view (flushing) and may only image the superficial layers of the artery wall (penetration depth 1-2 mm)[10–12]. To compensate for the limitations of each imaging modality, several hybrid intravascular IVUS-OCT systems have been developed for research purposes[13,14].

Both IVUS and intravascular OCT are mainly used to visualize the anatomy of the vessel. They may also indirectly detect some features associated with the presence of biological components inside atherosclerotic plaques such as calcification, lipids pools and thrombosis[12,15]. However, the ability of IVUS and OCT to reveal the underlying biology of atherosclerosis is limited by the physical mechanisms that determine their contrast: reflection of ultrasound or light from vessel structures. Recently, their limitations in assessment of plaque venerability status and identification of high-risk lesions have been highlighted in large-scale histology-based studies[16,17]

To attack the challenge of predictive atherosclerosis imaging, molecular methods have been widely proposed. In contrast to anatomical, molecular imaging can provide information about biological components of plaque that is essential for assessment of plaque vulnerability. Several molecular imaging modalities have been employed for the detection and characterization of atherosclerosis in vessels. For example, positron emission tomography (PET) has

been used for the imaging of plaque macrophages by use of F-fluorodeoxyglucose (FDG) agent[18]. Also, noninvasive detection of macrophages using a nanoparticulate contrast agent was demonstrated using computed tomography (CT)[19]. Finally, superparamagnetic iron oxides (USPIO) probe have enabled MRI detection of the human plaque inflammation[20]. However, all these modalities cannot offer sufficient resolution to detect critical parameters of CAD. Thus, high resolution intravascular imaging concepts have been introduced. Commercially available system from InfraReDx utilizes near-infrared spectroscopy (NIRS) to identify lipid core-containing coronary plaques[21]. In the research field, intravascular optoacoustic (IVOA) catheter was shown to localize lipid content[22]. Fluorescence lifetime imaging (FLIm) was reported to resolve pathological features including thin-cap fibroatheroma (TCFA)[23]. However, practicality of these approaches for clinical use is still under investigation.

At the same time, clinically demonstrated targeted fluorescence agents that could be employed for imaging biochemical and biomolecular disease in interventional cancer therapy[24,25] enabled new opportunities for imaging of biological processes associated with cardiovascular diseases. In a translatable step towards high resolution intra-arterial molecular imaging in clinical subjects, intravascular molecular imaging has been recently enabled by the development of a NIRF systems capable of two-dimensional imaging within human arteries[26].

Intravascular NIRF imaging is based on the injection of a fluorescent biomarker, which highlights a desired biological component or process via either active targeting, passive accumulation, or activation. Then, an intravascular NIRF catheter is employed to excite molecules using laser light of appropriate wavelength and collect fluorescence-emitted photons, which provide information about location and stage of disease. High sensitivity, ability to image through blood, and capacity to identify inflammation have been demonstrated in previous works[26,27].

Despite being useful for many applications, standalone NIRF is limited by two main drawbacks: first, standalone NIRF lacks morphological data, which is a key aspect of atheroma diagnostic and interventional therapy today. Second, due to the random position of the detector within a vessel and, thus, random optical attenuation caused by blood, NIRF amplitude, a crucial parameter for disease characterization, is distance-weighted and therefore only semi-quantitative. To overcome the morphological visualization and quantification limitations of standalone NIRF, images must be supplemented by precisely co-registered structural data that reveal the vessel anatomy and the distance between the catheter and the luminal boundary of the vessel. To address this challenge, a dual-modality intra-arterial catheter for simultaneous NIRF and OCT was first demonstrated by Yoo et al[28]. The reported system was shown to obtain detailed

co-registered molecular and morphological data, but only from a superficial layer of vessel wall. Additionally, OCT aspect required saline flushing and displacement of blood. More recently, *ex vivo* NIRF-IVUS imaging was demonstrated by fusing NIRF and IVUS images[29,30]. However, absence of information in the *in vivo* setting has limited the understanding of whether intravascular NIRF-IVUS imaging could be achievable and useful in living subjects.

In this work, we developed a pre-clinical cNIRF-IVUS system for intra-vascular imaging *in vivo*. Tide integration of ultrasound and high sensitivity fluorescence detectors into a single hybrid catheter allowed to simultaneously acquire molecular and morphological information. Precise co-registration of NIRF and IVUS components enabled us to account for NIRF light attenuation in flowing blood in *in vivo* settings. We hypothesized that IVUS-guided NIRF image reconstruction with a measurement-driven adaptive attenuation algorithm would yield rigorous quantitative readings of NIR fluorescence from the vessel wall. We experimentally interrogated the sensitivity, resolution, and quantification capacity of NIRF and IVUS components with phantom and *ex vivo* measurements. Then, we evaluated the ability of cNIRF-IVUS to detect *in vivo* accumulation of fluorescence agents in different clinical-relevant animal models of pathobiology, including fibrin deposition on coronary stents, atheroma-associated inflammation, angioplasty induced vascular injury.

3 Theory

3.1 Principals of Intravascular Fluorescence Imaging

This chapter will describe main principals of NIRF imaging and key effects involved in light propagation through tissue and blood. Focus will be on absorption (Error! Reference source not found.) and scattering (**3.1.2**) which are two the most fundamental interactions between photons and the molecules of biological medium. Close consideration will be given to optical properties of *in vivo* and *ex vivo* blood as it plays an important role in distance correction and quantification of fluorescence readings.

3.1.1 Basics of Fluorescence

Absorption of electromagnetic radiation is a phenomenon, when the energy of photon is transferred to an electron of the matter. The electron is excited by the gain in energy to a higher energy state. As excited state of an electron is unstable, it returns to its ground state by producing heat during non-radiative relaxation or by emitting another photon, which is called luminescence. The average time spent by an electron in the excited state is known as lifetime. Depending on lifetime, luminescence is divided into fluorescence (lifetime = 10^{-12}-10^{-7} sec) and phosphorescence (lifetime up to a several hours). Based on the law of conservation of energy, the energy of the emitted photon can only be lower

compared to absorbed photon. Since wavelength of the light is inversely related to photons energy, emission spectrum is always red-shifted relative to the excitation light's wavelength what is known as Stock shift phenomenon.

3.1.2 Effect of Absorption and Scattering in Biological Tissue

The probability of a photon being absorbed by a medium per unit path length is defined by the absorption coefficient μ_a[31]. Absorption coefficient is a characteristic of the medium but also a function of the photon's wavelength $\mu_a(\lambda)$.

The Beer-Lambert law can be derived from the definition of the absorption coefficient. It says that there is a logarithmic dependence between the intensity *I* of the light, which propagates through a substance and the product of the attenuation coefficient of the substance μ_a, and the distance the light travels through the material *d*:

$$I(d) = I_0 \exp(-\mu_a d) \qquad (1)$$

where, I_0 is the light intensity in the position *d*=0. Sometimes the probability of photon survival T_a is used. T_a is defined as

$$Ta(d) = \frac{I(d)}{I_0} \qquad (2)$$

Representative value for blood absorption coefficient is 100 cm^{-1}.

Scattering originates from interaction of photons with biological structures whose size is comparable with the optical wavelength and whose refractive index mismatches that of the surrounding medium[31]. Scattering forces photons to deviate from a straight trajectory and prevents transmission in ballistic regime. In biological imaging, scattering restraints light focusing what limits spatial resolution of the systems. It also results in longer pass length what, coupled with absorption, reduces light penetration.

Scattering property of the medium is described by scattering coefficient μ_s, which defines the probability of photon to scatter in a medium per unit path length. Same as absorption coefficient, scattering coefficient depends on the medium and photon's wavelength. The probability T_s of no scattering over path length d can be modeled based on Beer-Lambert law:

$$Ts(d) = \exp(-\mu_s d) \tag{3}$$

The extinction coefficient μ_t, also referred to as the total interaction coefficient, is given by

$$\mu_t = \mu_a + \mu_s \tag{4}$$

Its reciprocal is referred to as the mean free path between photon interactions.

3.1.3 Near-Infrared Optical Window

Compared to light in the visible spectral range, employment of near-infrared (NIR) light for biological imaging takes the advantage of absorption window in tissue where light exhibit maximum penetration depth. Generally, NIR optical window lays in the wavelengths range from 650 to 1350 nm where blood has minimal absorption. The dominant absorber in blood is hemoglobin. There are two different types of hemoglobin with different absorption spectra: oxyhemoglobin (HbO_2) and deoxyhemoglobin (Hb). While absorption of Hb generally decreases as light wavelength increases, HbO_2 has absorption minimum at around 690 nm. (**Figure 2**). Therefore, light in the spectral range of 650-800 nm is minimally attenuated by blood and tissues.
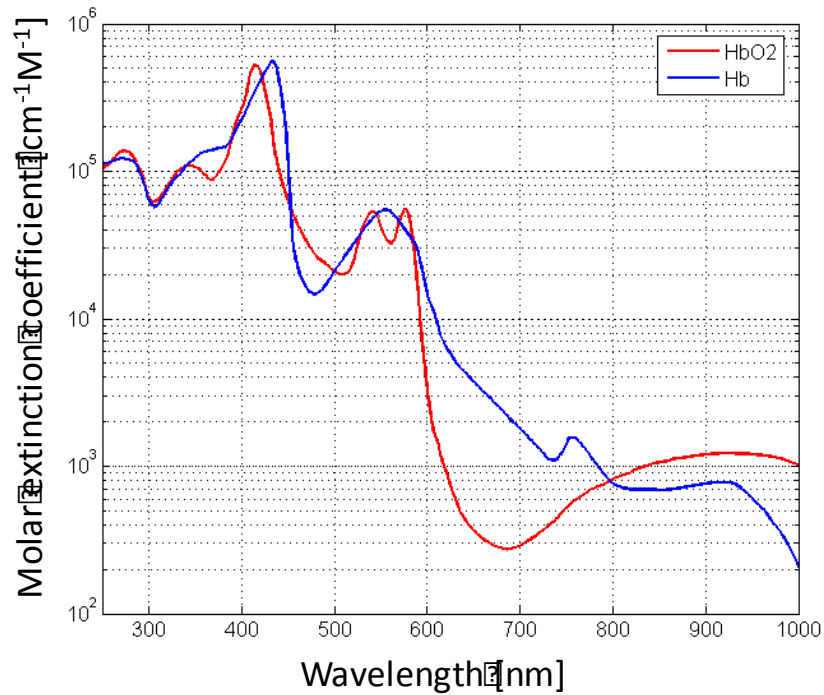
Figure 2. Absorption spectrum of oxy- and deoxygenated hemoglobin[32].

3.1.4 Modeling of Blood Optical Properties

The complete theoretical model used to study light-medium interactions occurring during photon propagation through tissue or blood is the *Radiative Transport Equation* (RTE). However, RTE is a very complex equation and has straightforward solutions only for very simple geometries. Thus, because of the complexity of the RTE, in practice approximations of the RTE are used. Additionally, *Monte Carlo* (MC) simulations are used to provide numerical solutions to the RTE. However, MC simulations require a lot of computing power and largely depend on accuracy of input parameters. Hence, approximations and models describing light propagation through tissue are preferable in many cases.

In case of light propagation through water or saline, the light scattering is neglectable and attenuation function $\alpha(r)$ could be approximated using the Beer-Lambert law. However, light propagation through blood is diffusive due to photon scattering. A more comprehensive model introduced by *Twersky* for transmission measurements[33] is often used to model light transmission through blood in biological applications[34–36]. It describes transmitted light intensity in terms of optical and physiological parameters of blood. Per this model, the distance-dependent attenuation function $\alpha(r)$ can be written as:

$$\alpha(r) = e^{-r(\mu_{a1}+\mu_{a2})}(e^{-B\omega(1-\omega)2r} + q(1 - e^{-B\omega(1-\omega)2r})), \quad (27)$$

where μ_{a1} and μ_{a2} are the absorption coefficients of blood for excitation and emission wavelengths, respectively, which could be found from the extinction coefficients, for example, in Bosschaart et al.[37], ω is the fractional hematocrit of blood which could be measured, *B* represents scattering, and *q* is a sensitivity parameter of imaging system. In case of NIRF measurement, *B* and *q* could be found by calibration measurements through curve fitting the experimental data to the expression given in **Eq.27**.

The reliability of values predicted using models depends foremost on accuracy of the input parameters such as μ_a, scattering *B* (which is formed by μ_s and scattering anisotropy *g*). In case of measurements in blood, these parameters are influenced by a large variety of factors of both physical and methodological

origin. Many groups have tried to quantitatively assess optical properties of blood[38–43]. One of the common challenges demonstrated was measurement conditions (i.e. blood flow and oxygenation state) that influence the optical properties of blood[40,44–47]. Also physiological parameters of donor have a significant influence on optical blood properties[48].

Generally, normal human blood is reported to consists of: (i) red blood cells – erythrocytes ($4500 \times 10^3/\mu L$), (ii) white blood cells – leukocytes ($8 \times 10^3/\mu L$), (iii) platelets - thrombocytes ($300 \times 10^3/\mu L$) and (iv) blood plasma. The volume percentage of red blood cells in blood is called hematocrit (*htc*). Normal *hct* level is 40% for adult woman and 45% for adult man. Red blood cells consist of hemoglobin (concentration 350 g/L). In healthy human adults, the average hemoglobin concentration in blood accounts for 140 g/L in women and 155 g/L in men[48]. But all these parameters, however, very significantly from one person to another.

Because red blood cells are the main contributor to the optical properties of blood (absorption contribution of two to three orders of magnitude higher than the other blood components), their characteristics like oxygenation level, volume percentage has direct influence on μ_a and μ_s. It is usually assumed that μ_a is proportional to *hct*. However, μ_s saturates for *hct* more than 10%. Thus, rescaling of the optical parameters to a different *hct* level introduces

inaccuracies. Nevertheless, there are equations, which allow to do that. One of them will be introduced below (see **Eq. 6** below).

Another effect which should be taken into consideration is absorption flattening: the phenomenon when absorption spectrum of a system with strongly absorbing particles (i.e. red blood cells in whole blood) is reduced compared to that of a suspension containing the same number of absorbing particles in homogeneous dispersion (i.e. haemolysed blood)[37,49,50]. Absorption flattening is one of the effects responsible for different optical behavior of *in vivo* blood compared to *ex vivo*.

A measurement of the blood scattering is in general methodologically difficult. Scattering in blood originates from the complex refractive index mismatch between red blood cells and plasma. Usually, plasma is replaced by saline or phosphate buffer in *ex vivo* blood phantoms, which increases refractive index mismatch and leads to scattering overestimation. In addition to that, absorption and scattering are highly dependent on oxygenation level of blood[42,51].

As mentioned before, rescaling equation of the scattering coefficient from one *htc* to another is not trivial. Approaches for achieving this were suggested in several studies[33,52]. However, the most accurate one was introduced by Bosschaart et al.[37] They computed the hematocrit-dependent scaling factor $\gamma(htc,\lambda)$ at each wavelength (250-2000 nm) and averaged it over measured

spectrum using a Levenberg Marquardt non-linear least squares curve fitting procedure. This resulted in the following approximation of the hematocrit-dependent scaling factor:

$$\gamma(htc) = (1 - htc)(0.98 \pm 0.02 - htc) \approx (1 - htc)^2 \qquad (5)$$

Equation 5 can be used to scale μ_s to different hematocrit levels:

$$\mu_{s,htc} = \frac{\gamma(htc2)}{\gamma(htc1)}\frac{htc2}{htc1}\mu_{s,htc1} \qquad (6)$$

The challenge of measuring optical properties of *in vivo* blood could be also addressed empirically, if transmitted optical intensity is measured simultaneously with thickness of circulating blood through which light travels. Then, the coefficient of total interaction μ_t could be calculated using **Eq. 4**. However, a proper instrumentation which would allow simultaneous measurement of distance and light intensity is required. In the **Chapter 5** of this work hybrid cNIRF-IVUS system which enables such measurement is described.

3.2 Principals of Ultrasound imaging

This chapter will start with definition of two basic acoustic parameters: acoustic impedance and transmission coefficient. These two parameters play a major role in acoustic wave propagation in multilayer structures. Herein, they will be introduced based on acoustic linear wave equation. In this work, careful

consideration was given to acoustic impedances of catheter materials to provide

good acoustic matching and enable adequate image quality. Next, principals of

ultrasound transducer will be introduced in Section **3.2.2**. Then, in the Section

Error! Reference source not found., parameters of ultrasound imaging will be d

iscussed, i.e. scanning modes, resolution, scan speed and pulse rate, image

artifacts, and noise sources.

3.2.1 Introduction of the Differential Wave Equation.

Acoustic wave can often be considered as a longitudinal wave, which creates a

sinusoidal back-and-forth motion of media particles. Particles move around their

equilibrium with a displacement amplitude *u*, at a velocity *v*, and frequency *f*.

These movements also correspond to a local pressure disturbance *p*. The time *t*

which wave takes to propagate for a distance *z* is determined by the longitudinal

speed of sound C_l:

$$t = \frac{z}{C_l} \tag{7}$$

Such a wave has a wave number k_l defined as

$$k_l = \frac{w}{C_l} \tag{8}$$

where $w = 2\pi f$ is the angular frequency. The particle velocity is related to its

displacement as

$$v = \frac{\partial u}{\partial t} \tag{9}$$

For convenience, a velocity potential ϕ is defined such as

$$\nabla\phi = v \tag{10}$$

Then, pressure can be defined as

$$p = -\frac{\rho\partial\phi}{\partial t} \tag{11}$$

where ρ is the density of the fluid at rest. Finally, pressure created by a harmonic

wave can be described as

$$P(w) = -iw\rho\phi(w) \tag{12}$$

There are many forms of the wave equation. Using parameters introduced above

it can be represented in differential equation

$$\frac{\partial^2\phi}{\partial z^2} - \frac{1}{C_l^2}\frac{\partial^2\phi}{\partial t^2} = 0 \tag{13}$$

The ratio of pressure to the particle velocity at a single frequency is called specific

acoustic impedance (sometimes called shock impedance) and is expressed in

Rayls ($Rayl = kg/m^2 sec$). Therefore

$$Z = \frac{\rho}{v} = \rho C_l \tag{14}$$

Now, we can consider a common situation when acoustic wave is propagating in

a medium with acoustic impedance Z_1 bouncing off a boundary of different

impedance Z_2. Local particle pressure as well as velocity must be continuous across the boundary. From this, the intensity of incident wave can be calculated. If Z_1 and Z_2 are known, following equation can be used to calculate the fraction of the incident wave intensity that is reflected:

$$R = \frac{(Z_2 - Z_1)^2}{(Z_1 + Z_2)^2} \tag{15}$$

In **Eq. 15,** R is known as the *reflection coefficient*. The amplitude of the wave transmitted through the boundary will be

$$T = (1 - R) = \frac{4Z_1 Z_2}{(Z_1 + Z_2)^2} \tag{16}$$

T is known as *transmission coefficient* and often used to calculate losses in ultrasound systems (like intravascular catheter), which consists of different materials. It is also used in transducer design to identify proper materials for matching and backing layers of the transducer.

3.2.2 Characteristics of Ultrasound Transducer

In ultrasound transducer, a wave is created by applying a short voltage pulse to the piezoelectric crystal. The central frequency of the created wave is determined by resonance frequency f_0 of the piezoelectric block:

$$f_0 = \frac{C}{2d} \qquad (17)$$

where C is the sound speed in the piezoelectric material, d is the thickness of the block.

For enhanced sensitivity, shorter pulse duration, reduced reverberation (ring-down) time, and broaden bandwidth, the piezoelement is squeezed between backing and matching layers. **Figure 3** illustrates schematics of an ultrasound transducer. Backing material should absorb as much of back propagating acoustic wave as possible. Therefore, per **Eq.16**, it's acoustic impedance Z_b should be equal to that of the piezoelectric ceramic (matching impedance condition, $T \sim 1$) and at the same time should present high acoustic attenuation coefficient α. Usually, polymers are used as backing material, but recently, different composite materials have demonstrated good matching results. Among them are polymeric resins combined with metallic particles of silver, gold, oxide of lead or tungsten[53,54].
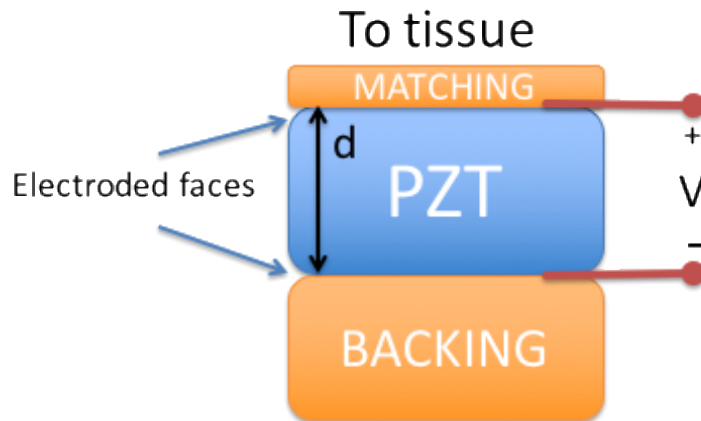
Figure 3. Schematics of an ultrasound transducer. To create acoustic wave, short voltage (V) pulse is applied to a piezoelectric block (PZT). Frequency of the excited wave depends on thickness of the PZT block d.

One of the main parameters of the transducer is a transmission factor *TF*, which describes how well acoustic energy is transferred from a piezoelectric crystal to adjacent material (water, tissue, blood). It and can be calculated from on **Eq.(16)**. The typical value of acoustic impedance for PZT is 34 MRayls. Acoustic parameters (density, speed of sound, and acoustic impedance) of some biological and non-biological materials obtained from literature[55] are presented at **Table 1.**

Tissue or Material	Density (g/cm³)	Speed of Sound (m/sec)	Acoustic Impedance [kg/(sec·m²)]x10⁶
Water	1	1480	1,48
Blood	1,055	1575	1,66
Fat	0,95	1450	1,38
Liver	1,06	1590	1,69
Kidney	1,05	1570	1,65
Brain	1,03	1550	1,6
Heart	1,045	1570	1,64
Muscle	1,065	1580	1,68
Skin	1,15	1730	1,99
Eye lens	1,04	1650	1,72
Bone	1,9	4080	7,75
Teeth	2,2	3600	7,92

Table 1. Acoustic parameters of some biological and non-biological materials. [55]

If, for example, PZT is excited in water (1,48 MRayls), *TF* will be only 18% due to acoustic mismatch between crystal and water. To minimize reflections caused by ultrasound mismatch and improve efficiency, single or multiple matching layers are usually placed on the front surface of the PZT. For the best coupling, acoustic impedance of the matching layer Z_m should be the geometric mean of the piezoelectric material Z_c and the imaging tissue Z_t [56]:

$$Z_m = \sqrt{Z_c Z_t} \qquad (18)$$

The matching layer usually has a quarter wavelength of central frequency and the acoustic impedance of 3-15 MRayl, depending on which piezoelectric

material used. Solid particle polymer composites are widely used as a matching material today allowing *TF* to be as high as 90%.

3.2.3 Modes of Ultrasound Imaging

Ultrasound transducers are used to visualize composition of the tissue using pulse-echo mode. When received echo signal from a single transducer is visualized as function of depth, it is called *A-mode* (amplitude-mode) signal. If the *A-mode* signals are registered over a plane through the tissue by either scanning or by using a linear array of transducers, a two-dimensional image can be formed. This is called *B-mode* (2D-mode). In *M-mode* (motion-mode) ultrasound signals are recorded over time in either *A-mode* or *B-mode*. This way, motion of organs and structures can be imaged.

Intravascular ultrasound with a rotating single element transducer utilizes *B-mode* imaging. During rotation echo signals from different directions in one cross-sectional plane are detected and then visualized in polar coordinates. Through the linear translation of the transducer perpendicularly to the imaged plane after every 360-degree rotation, three-dimensional volume can be imaged. However, to increase pullback speed, helical scans are often used for intravascular ultrasound. Due to relatively small pitch size (smaller or

comparable with lateral resolution of the transducer), helical pullback could be approximated as plane-by-plane scan during image reconstruction.

Generally, rotating transducer inside a vessel should be enclosed inside a protective tube during all time. There are multiple challenges associated with such a tube, including

1. Tube should be transparent for ultrasound waves. Therefore, per **Eq.16**, catheter material should have acoustic impedance close to saline or blood (1.5-1.6 MRayl). At around 40 MHz such materials as thin-walled low-density polyethylene (LDPE, 1.95 MRayl) and polymethylpentene (PMP, TPX, 1.84 MRayul) are the most suitable since they introduce ~30% one-way losses of ultrasound energy.

2. If the same catheter is also used for optical imaging (as in case of cNIRF-IVUS system, see **Chapter 5**), catheter should be optically transparent at excitation and emission wavelengths.

3. Furthermore, as ultrasound energy cannot be transmitted by air, catheter should be filled with water or acoustic matching fluid, which is transparent and has good transmission characteristics for ultrasound. Air bubbles inside the catheter will make it "blind" during operation. Considering the possibility that fluid can leak into the blood stream, choices of the fluid are

limited to bio-compatible water-based solutions like saline and distilled water.

The challenges above have been successfully addressed in this work as described below.

3.2.4 Ultrasound Resolution and Penetration Depth

The smallest distance at which two objects are identified separately characterizes the resolution of an ultrasound imaging system. The axial resolution (*AR*) is defined in the direction of ultrasound beam propagation, while the lateral resolution *LR* in the perpendicular direction to the ultrasound beam.

In intravascular imaging, usually unfocused ultrasound detectors are used. Thus, as was introduced in **3.2.2**, the *AR* is related to the length of the pulse-wave, which depends on backing quality, frequency f_0 and sound velocity in the surrounding media *C*. It could be estimated as 1.5 wavelengths:

$$AR = 3\frac{C}{2f_0} = \frac{3\lambda_0}{2} \tag{19}$$

The *LR* is given by the beam width at specific distance from the transducer and typically defined by -3 dB beam contour. *LR* depends on transducer parameters including shape and size, central frequency, presence of focusing lens. Beam shape of an unfocused transducer is schematically presented in **Figure 4**.
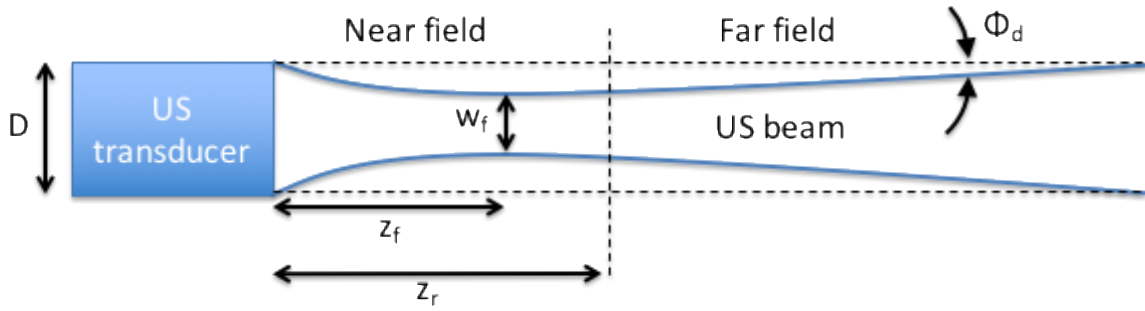
Figure 4. Shape of the ultrasound beam created by a round unfocused transducer. D is a diameter of the transducer, w_f – width of the beam in focus, Φ_d - divergence angle of the beam, z_f and z_r are focal and far field distances, respectively.

Near field ($z < z_r$, where z_r is far field distance) of a transducer is characterized by an irregular pattern of the ultrasound intensity. It is formed by interference of ultrasound waves originating from different parts of the aperture. In the region around $z = z_r$ far field conditions start to develop. Distance z_r can be calculated as

$$z_r = \frac{D^2}{2\lambda} \tag{20}$$

Further away from the transducer ($z > z_r$) far filed starts. Far field is characterized by a diverging Gaussian beam with half-angle Φ_d. The point where beam has a minimal width w_f is called focal point. It is located on the distance z_f from a transducer:

$$z_f \approx 0.8z_r \tag{21}$$

$$w_f \approx 0.5D \tag{22}$$

34

$$\Phi_d \approx \arcsin\left(\frac{0.52\lambda}{D}\right) \tag{23}$$

Imaging is typically done using far field of the transducer. Thus, lateral resolution *LR* on the distance *z* can be estimated as

$$LR = w_f + 2\left(z - z_f\right)\tan(\Phi_d) \approx w_f + \frac{1{,}04(z - z_f)\lambda}{D} \tag{24}$$

Per **Eq.(19)** and **Eq.(24),** *AR* and *LR* increase with frequency of the transducer as it is illustrated in **Figure 5**. Based on **Eq.(20)**, higher frequency also allows for a smaller size of the transducer *D* at constant near field length z_r. A higher frequency, however, reduces penetration depth of the US beam and consequently the depth of view. So, the frequency of the transducer for each imaging application should compromise resolution, size of the transducer and penetration depth.
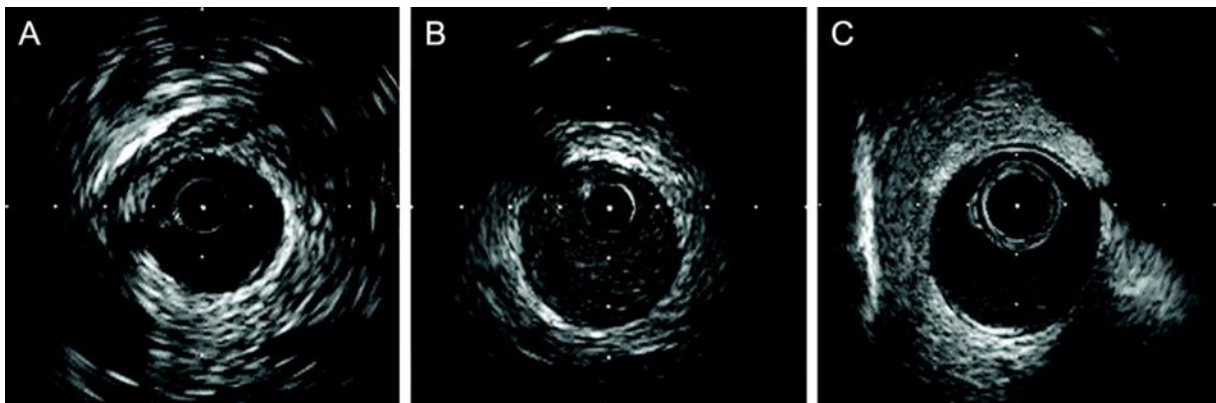

Figure 5. IVUS images at 30, 40, and 50 MHz. IVUS images of a coronary artery at (a) 30 MHz, (b) 40 MHz, and (c) 50 MHz. The higher center-frequency images have better axial resolutions but less penetration depth[57].

For the intravascular ultrasound imaging it is important to clearly determine the lumen contour of the vessel and distinguish between anatomical layers inside the vessel wall. This requires a high *AR* of about 0.1 mm while the *LR* is less important. Required penetration depth is 5-10 mm. As an example, unfocused disk-shaped round PZT transducer with diameter of 0.8 mm and central frequency 40 MHz meets such requirements. Per the theory above, such a transducer can offer *AR* of about 0.06 mm if good backing is achieved and *LR* of 0.4-0.8 mm. The divergence angle Φ_d is as small as 1.5 grad. However, penetration depth will be limited to about 9 mm, which is not enough for big arteries like aorta (10-15 mm inner diameter). Therefore, for big vessels, lower central frequency should be chosen to image the whole cross-section. 15-20 MHz may be a convenient frequency for such application.

3.2.5 Noise Sources and Artifacts in Intravascular Ultrasound Imaging

There are three main sources of artifacts in ultrasound images, which will be discussed in this section: motion artifacts, electromagnetic interference and catheter tip motion. All result in distortions, which make the interpretation of acquired information challenging and limit our understanding of the vessel morphology.

In vivo heart pulsates with frequency of about 1 Hz in humans and about 1.3 Hz in swine. Pressure pulses are transmitted through vessels to peripheral arteries. There are also lower frequency respiratory motions. In case of intravascular imaging, both motion mechanisms result in image artifacts. If the disposition between frames is small enough (fast rotation), image artifacts will be neglectable. From the other hand, faster speed of rotation reduces the number of pulses per rotation. This, sequentially, limits available data for averaging needed for adequate signal-to-noise ratio (SNR) of ultrasound (and optical-NIRF) images. Current commercial systems allow IVUS imaging at framerate of 30 fps. Still, however, images sometimes suffer from motion artifacts[58,59].

Electromagnetic interference comes from the interaction of the system parts with radiation of radio frequencies from the environment. Thus, IVUS system operating on high frequency incurs electromagnetic interference with all kinds of sources of radio waves. Every unshielded part of the detecting module acts as an antenna that receives electromagnetic signals. Those appear as random noise or periodic radial lines and arcs in the acquired images. As an example, an A-line signal from one angular projection and a resulted cross-sectional B-scan with parasitic RF-interference is illustrated in **Figure 6**.
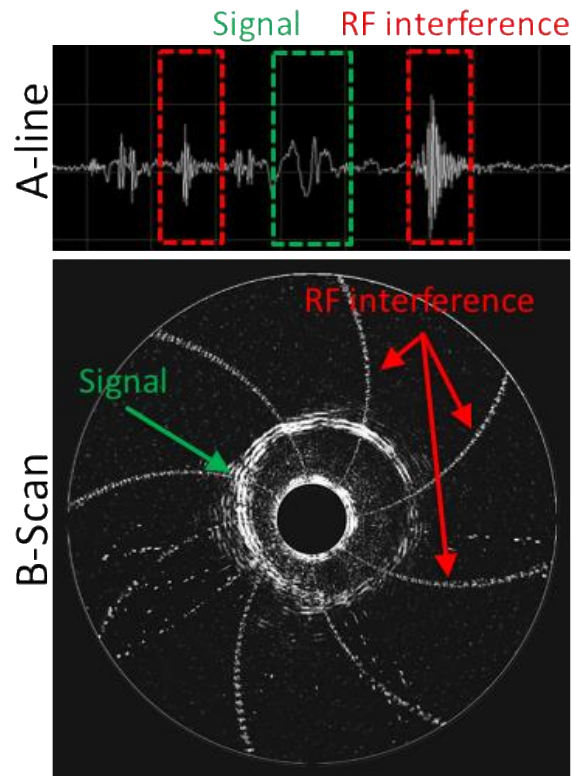
Figure 6. Effect of parasitic RF interference on an ultrasound image.

Electro-motors, drivers and switching power suppliers usually act as strong sources of noise. To minimize electromagnetic interference, the system should be equipped with a good grounding circuit. All high frequency connectors should be shielded and grounded. Also, high frequency shielded coaxial cables should be used for signal transmission. Important to note, that attenuation of high frequency signals as well as noise power increases with length of cables.

Unpredictable catheter tip motions also affect the reliability of the images. Each image line is defined by the received echo signal and its location of origin. The reconstruction is based on several assumptions:

1. The location of origin, which is associated with a transducer position, is assumed to not change during one revolution. This means that no radial or tangential motion of the catheter tip occur with respect to the blood vessel wall.

2. Transducer is assumed to rotate with uniform velocity, which insures correct angular representation of the vessel.

3. Exact and known number of ultrasound pulses should be emitted and distributed evenly during one revolution.

However, these assumptions are not generally valid. Radial and tangential motions of the catheter tip usually originate from motion of the blood vessel because of heart beat and breathing. Due to friction between protective catheter and electrical wires and ultrasound transducer, rotation with non-uniform velocity often occurs. Finally, velocity imprecision, rotation acceleration and deceleration leads to unequal number of projections within each revolution[60].

4 NIRF System for Intravascular Imaging

In interventional cardiology, the most widely used *in vivo* imaging modalities are IVUS, OCT and X-ray angiography. Despite their great ability to visualize morphological features of the vessels, they are limited in the capacity to detect molecular components and features of atherosclerosis. Several systems with molecular sensitivity have been introduced to address this challenge, i.e. near-infrared spectroscopy (NIRS)[64], fluorescence lifetime imaging (FLIm)[23], optoacoustics[65], and near-infrared fluorescence (NIRF)[26]. While the first three rely on intrinsic fluorescence contrast to distinguish between plaque components like lipid pools, collagen, or elastin, NIRF takes advantage of specifically designed exogenous fluorescence agents to detect a variety of specific molecules or processes including plaque formation[66], protease activity[67–70], oxidized low-density lipoprotein content[71], plaque permeability[66,68], or fibrin deposition[68].

In this work, we further investigated the ability of NIRF to detect accumulation of a novel fluorescent marker with affinity to endothelial cells. Therefore, high sensitivity NIRF catheter for intravascular imaging was engineered. Spectral response of the setup was optimized to match the emission spectrum of the fluorescent marker. Sensitivity and resolution was characterized in phantom experiments. Finally, ability to detect endothelial integrity in vessels was

demonstrated *ex vivo*. NIRF imaging results were corroborated by fluorescence microscopy.

4.1 Description of the NIRF Setup

Schematics of the NIRF system is shown in **Figure 7**. Setup employed a continuous wave (CW) laser source (B/W Tek Inc., Lübeck, Germany) for fluorescence excitation. Depending on which fluorescent agent was imaged, different lasers operating on central wavelengths 660 nm, 750 nm or 780 nm were used. Light from the laser was coupled into a multi-mode (MM) fiber (Thorlabs, M74L01) through a free space arrangement. MM fiber was connected to an imaging fiber by means of a custom-made rotary joint (Princetel, Inc, NJ, USA; **Figure 7** inserts on bottom right) which allowed optical interface between rotating catheter and stationary part of the system. Catheter rotated inside a protective plastic sheath. Laser power on the tip of the catheter was 15-25 mW depending on alignment parameters. Fluorescence emission light was captured by the same side-viewing catheter. A dichroic mirror (DM) (AHF Analysentechnik AG, Tübingen, Germany) included into the free space arrangement reflected captured fluorescence towards optical filters. Filters set was chosen accordingly to excitation and emission wavelengths of the fluorophore. Finally, NIRF signal was detected by a photomultiplier tube (PMT; H5783-20, Hamamatsu Photonics,

Shizuoka Pref., Japan). Output signal of the PMT was digitized with sampling rate of 60 MS/sec using analog to digital converter sampling card (NI PCI-5124, Munich, Germany).
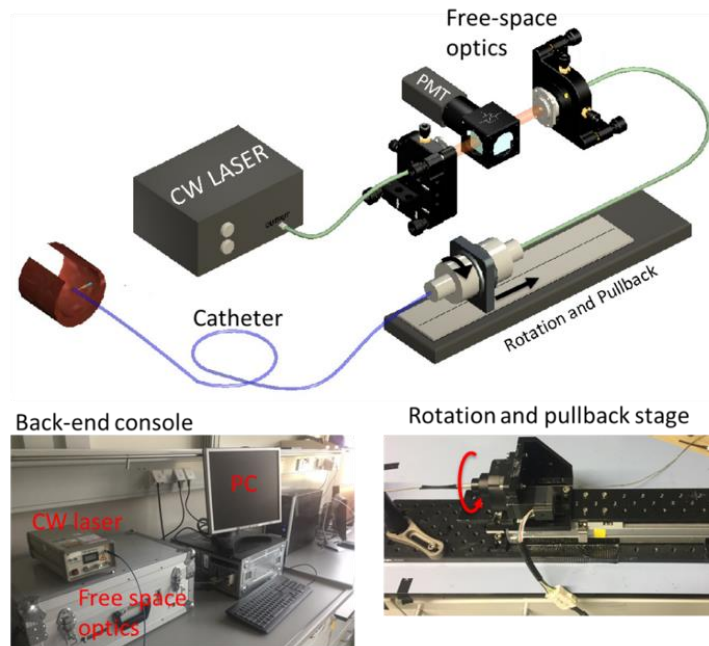
Figure 7. Schematics of the NIRF system.

To automatically rotate and pullback the catheter, rotary joint (**Figure 7** inserts on bottom right) was equipped with a motor for rotation and mounted on a translational stage (Orienal Motor co Ltd, model EZ Limo and VEXTA). This allowed catheter to be helically rotated at rotation speeds of up to 200 revolutions per minute and translated along the vessel with an adjustable pitch size of 0.2 - 0.5 mm per rotation.

4.2 Engineering of the NIRF Catheter

The emitted from the catheter laser beam was a diverging cone with aperture determined by core size and numerical aperture (NA) of the fiber and by scattering coefficient of the surrounding media. Dimensions of this cone defined NIRF resolution and sensitivity. We computed the theoretical resolutions in saline for catheters based on three different fibers: 100 µm core, NA=0.39; 200 µm core, NA=0.22; and 400 µm fiber, NA=0.39 (**Figure 8**). As a first order approximation, saline was assumed to have no scattering and photons to travel in a ballistic regime. In such a case, the beam can be considered a parallel bundle of wave-fronts that diverges per angle defined by NA.

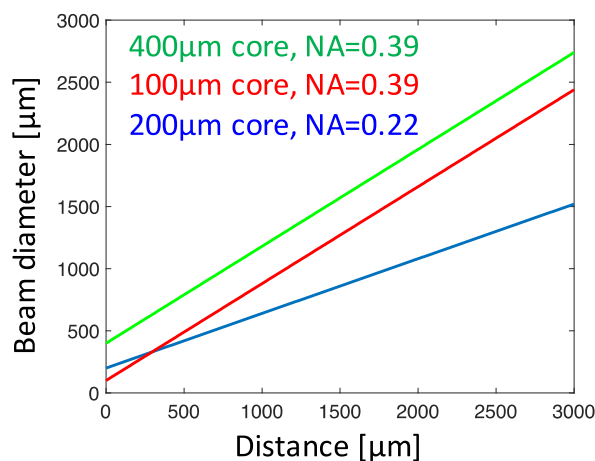Figure 8. Simulations of the beam diameters for three types of NIRF fibers. Fiber with a core size of 200um and NA=0.22 showed a good compromise between core diameter and beam size which determines resolution of the catheter.

Results indicated that catheter based on a fiber with 200 µm core and NA=0.22 offers a good compromise between resolution determined by a beam diameter and sensitivity dependent on core size.

Next, we build a NIRF fiber assembly which is illustrated in **Figure 9**. Assembly consisted of a 200 μm core, NA=0.22 MM fiber (Thorlabs, FT400EMT) with 45-deg prism (Precision Optics Corporation, Gardner, MA USA) glued on the distal tip of the fiber to reflect light perpendicularity to the fiber axis. Fiber optics was fixed inside a stainless-steel ferrule for mechanical protection. Proximal tip of the MM fiber was connectorized with standard FC-PC connector. During imaging assembly was rotating inside a stationary catheter tube made of polyethylene (PE). Total outside diameter of the catheter was 1.5 mm (**Figure 9d**). Tube was additionally equipped with x-ray markers for angiographic guidance and a monorail port for introduction into the vessel via clinical monorail system.
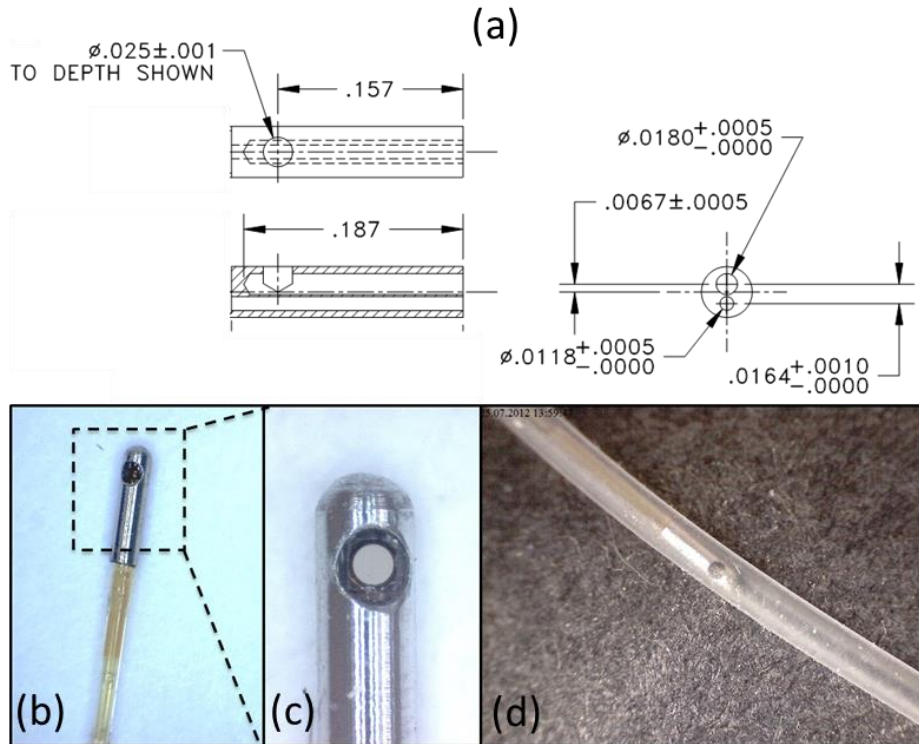
Figure 9. NIRF catheter. (a) Blueprint of the NIRF ferrule. (b) NIRF catheter assembly. (c) Zoom-in view of the NIRF catheter assembly shows a prism glued on the distal tip of the 200 μm core optical fiber. (d) NIRF catheter housed within a protective polymer sheath.

4.3 Data Acquisition and Image Reconstruction Algorithm

Analog to digital converter had 256 MB onboard memory. To avoid overwriting of un-fetched data and, thus, to increase stability of the data acquisition system, a producer/consumer design pattern was realized in LabVIEW environment. This allowed enhanced data sharing between multiple loops running at different rates: data fetching from the analog to digital converter and data writing to HDD. The producer/consumer pattern was used to decouple processes that produce and consume data at different rates. Data queues were used to communicate

data between loops in the producer/consumer pattern. These queues offered the advantage of data buffering between fetching and writing. Acquired NIRF data was then stored as a 16-bit binary file in the directory defined by operator. A separate binary file was created to contain metadata including sampling rate, travel range, step size, RPM, etc.

All data post-processing was performed offline in MATLAB. First, mean averaging and down sampling was performed so that one revolution was composed of 400-500 data points (**Figure 10**). This allowed improved SNR. Then, using metadata, signals were reshaped into two-dimensional matrix where vertical axis represented pullback dimension and horizontal axis represented the angle scanned within each pullback position. Finally, two-dimensional image was reconstructed in polar coordinates using black-blue-green or 'hot' colormap.
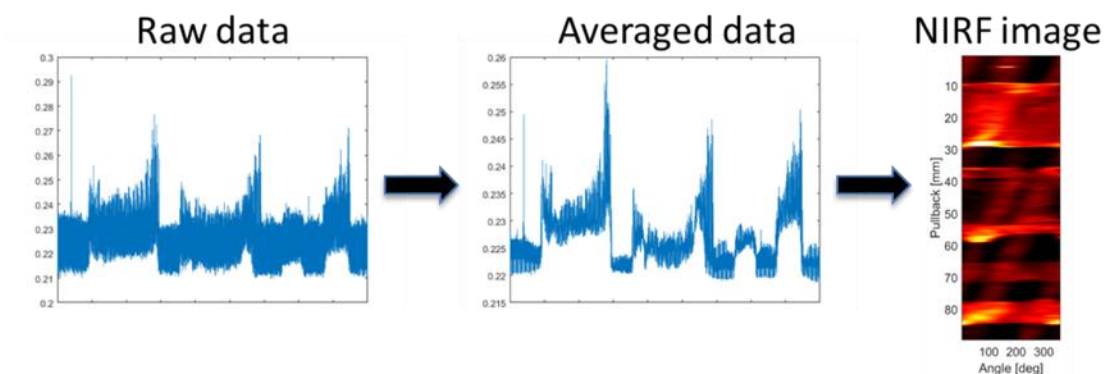

Figure 10. Steps of NIRF image reconstruction.

4.4 GUI for Data Acquisition Control

System control, data acquisition, signals pre-processing and visualization was implemented in LabVIEW environment (LabVIEW 2011, National Instruments, Germany). Screen-shot of the graphical user interface is presented in **Figure 11**. It consisted of four main sections based on workflow. Section 1 was used to set a directory and a name of the data file. Section 2 was responsible for pullback parameters: *Linear Travel Range* (pullback distance in mm), *Step size* (pitch length in mm), *RPM* (speed of rotation in rounds per minute). Switch *Move* was used to toggle between pullback and static operation of the system. Section 3 was used to set-up acquisition parameters such as *Chanel Name* (name of the data channel connected to the NIRF detector, channel 1 or channel 2), *Min Sampling Rate* (data sampling rate), *Max Points Per Fetch* (number of sampling points fetched from the acquisition card simultaneously), *Max V* (maximum amplitude of the signal). Indicators *Last Point Fetched* and *Total Points Fetched* were used to display number of data points acquired and were useful for system control.

Since sampling rate of the data acquisition was as high as 60 MHz, it was often a case that data was fetched faster than it could been written to the HDD. To avoid such condition, on-fly data averaging was used. Parameter *AVG F* set an on-fly averaging frequency in Hz. Also, data buffer was created to keep fetched data

points before they can be written to HDD. Field *in queue* showed number of fetches stored in buffer.

Section 4 of the graphical user interface was a display section. It consisted of a *Waveform Chart* for display of acquired signal in real time for visual monitoring. Indicator *Progress* showed a real time pullback progress.
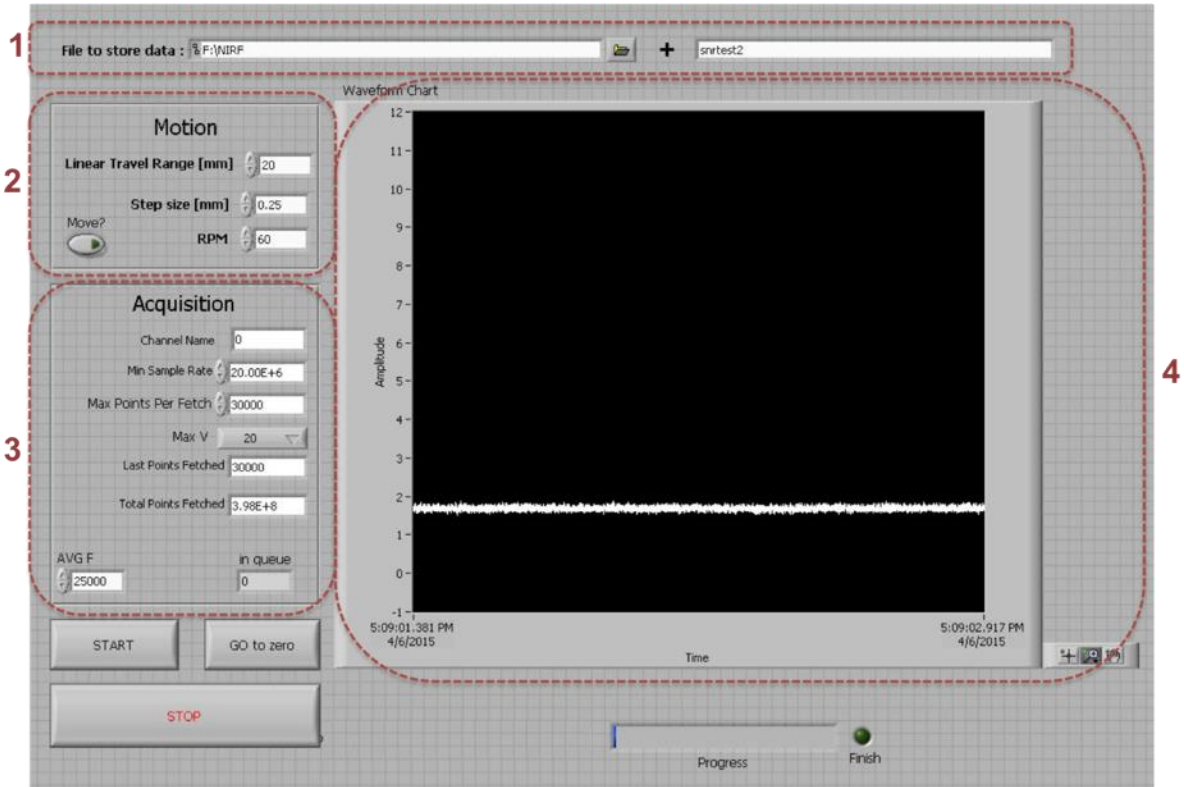

Figure 11. GUI for NIRF system control. Section 1 – file name; Section 2 – pullback parameters; Section 3 – acquisition parameters; Section 4 – real time display.

4.5 Characterization of NIRF Resolution and Sensitivity

To characterize imaging parameters of the catheter, first, full width at half maximum (FWHM) of the NIRF beam was assessed. Therefore, beam profile was measured at multiple distances in the range of 0 – 50mm with a step of 5mm (**Figure 12a and b**). Inserts in **Figure 12a** shows representative beam photographs 0mm, 25mm, and 50mm away from the catheter. In the 0-3mm range - FWHM was measured with a finer step of 100µm (**Figure 12c and d**).

As shown in **Figure 12** beam size increased linearly with distance in accordance to the divergence angle defined by NA=0.22. At 1mm distance FWHM was measured to be 0.67mm. Measured values agree well with simulations shown in **4.2**.
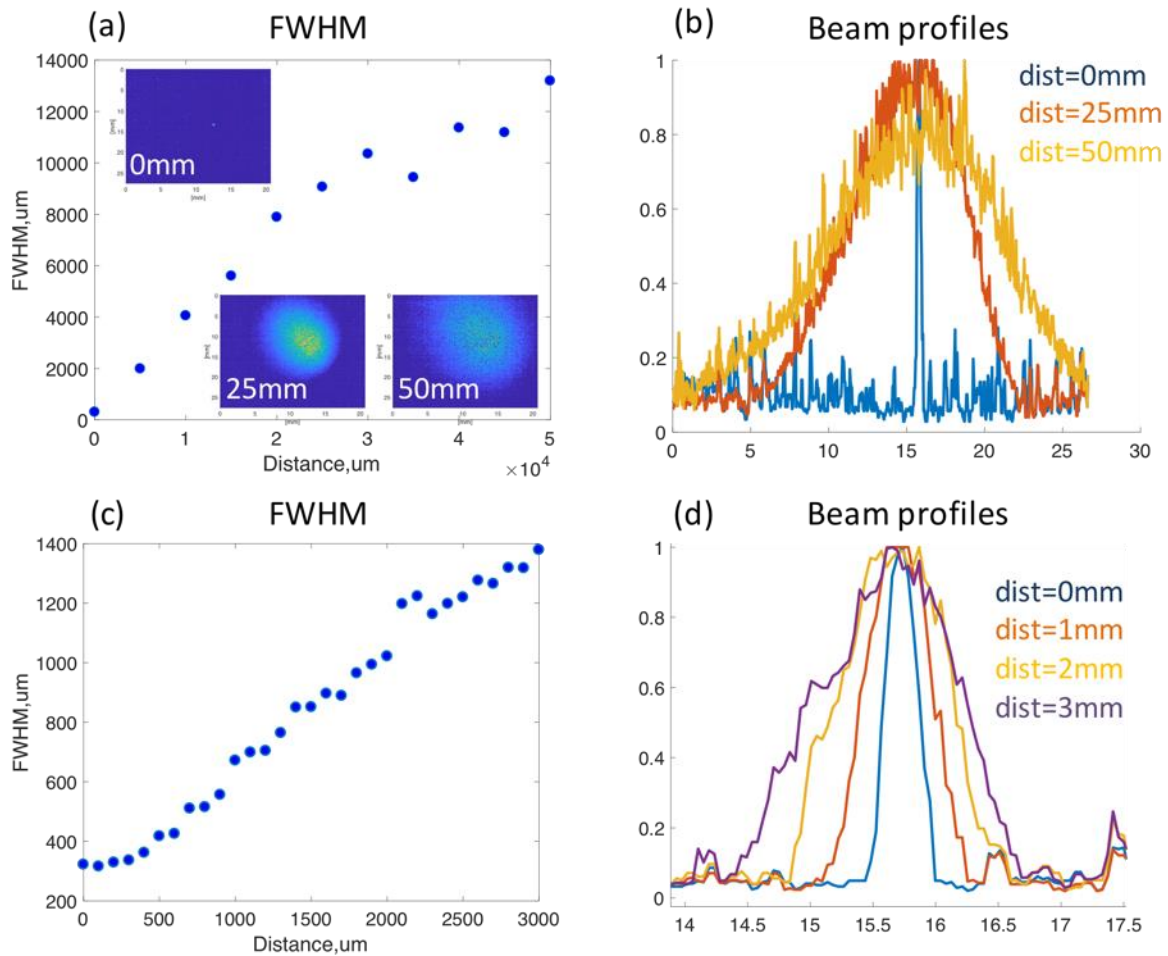
Figure 12. NIRF beam FWHM characterization. (a) FWHM as function of distance from the catheter in the range 0mm - 50mm. Inserts show representative beam cross sections at 0mm, 25mm, and 50mm distances. (b) NIRF beam profiles at distances 0mm (blue), 25mm (orange), and 50mm (yellow). (c) FWHM as function of distance from the catheter in the typical imaging range 0mm – 3mm. (d) NIRF beam profiles at distances 0mm, 1mm, 2mm, and 3mm.

To assess lateral resolution of the NIRF catheter in more realistic imaging scenario we measured minimal distance at which two objects are resolved at distances 0.5-1.5mm. Therefore, we build a fluorescent cross phantom as shown in **Figure 13**. It was constructed from two crossed polyethylene tubes 1 mm in diameter filled with a fluorescence dye AlexaFluor750 (200 mg/ml, Ex./Em.

749/775 nm; **Figure 13b**). Phantom was placed inside a water bath and scanned

using NIRF catheter.
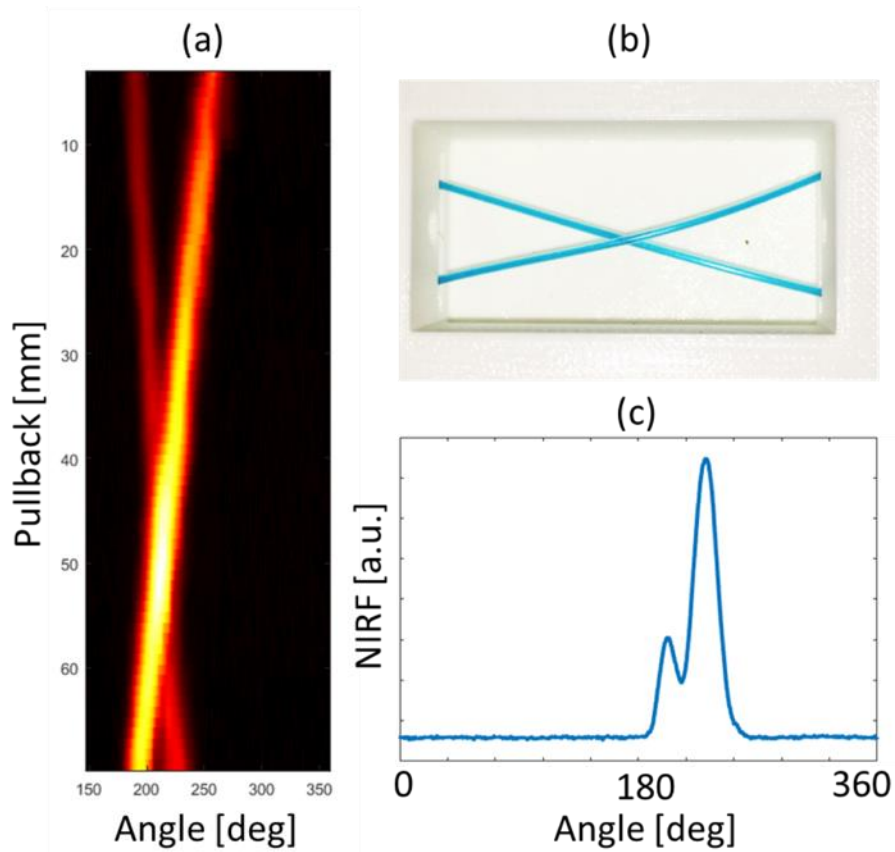
Figure 13. Measurement of NIRF lateral resolution. (a) NIRF image of the fluorescent cross phantom. (b) Photograph of the fluorescent tube phantom. (c) NIRF signal from a fluorescent tube phantom at pullback position 34mm.

We identified minimal lateral distances at which two tubes are still resolved

based on NIRF data. **Figure 13a** shows acquired NIRF image of the phantom.

Figure 13c depicts NIRF signal at pullback position 34mm. As a result, NIRF lateral

resolution was estimated to be 460 μm.

To measure sensitivity, we sequentially filled a transparent tube (outside diameter OD=1mm, inside diameter ID=0.7mm) with AlexaFluor750 at different concentrations (50nM, 200nM, and 500nM). Tube was placed inside a bath filled with saline at an angle of about 30 degrees respectively to the NIRF catheter and sequentially scanned. This way NIRF signal through different distances in saline was detected (**Figure 14a**). Fluorescent tube with dye at concentration 500nM was also measured through *ex vivo* blood (**Figure 14a,** purple dots). Normalized NIRF signals from the florescent tube phantom through 1mm and 2.2mm of blood are illustrated in **Figure 14b** with blue and red lines, respectively.
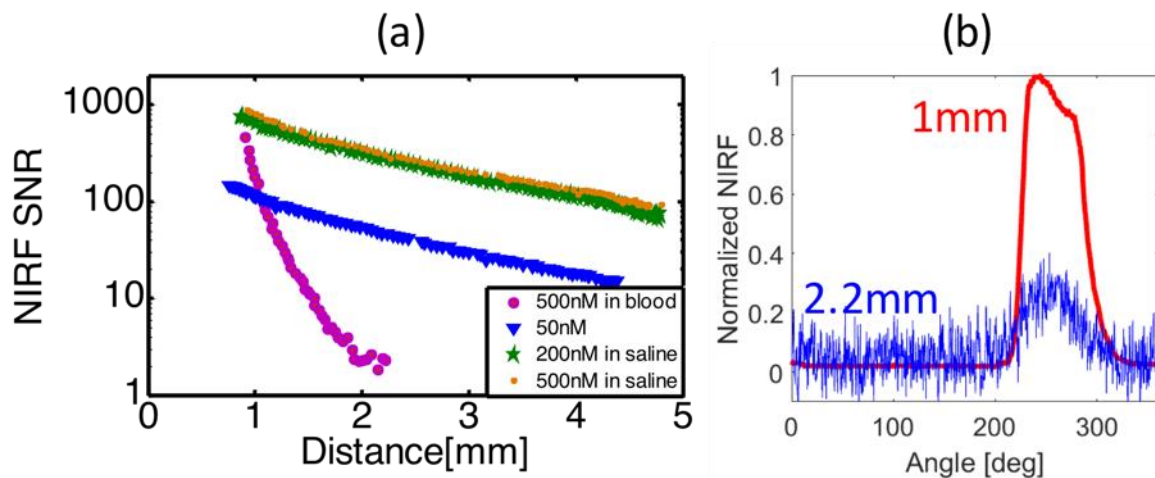

Figure 14. NIRF SNR measured in blood and saline.

Overall, higher absorption and scattering properties of blood resulted in faster SNR decay with distance. However, 500 nM concentration of the dye was detected at a fiber-to-target distances up to 2.2 mm in *ex vivo* blood. In saline,

all measured concentrations of AlexaFluor750 were reliably detected at distances up to 4.7mm from the catheter.

Results demonstrated herein showed that engineered NIRF catheter based on an optical fiber with 200 µm core and NA=0.22 offers a typical lateral resolution of 0.67mm when imaging in saline or air. In blood, resolution will strongly depend on distance between catheter and vessel wall and scattering parameters of blood (hematocrit, cholesterol level, etc.). Based on previous experience, it can be roughly approximated by doubled resolution in saline.

SNR in saline was shown to be >15 at distances up to 4 mm what is sufficient for imaging in vessels with diameters up to 5-6 mm. In case of imaging through blood, SNR was more than 2 for distances up to 2.2mm, what allows reliable imaging of vessels up to 3-4mm in diameter.

To choose a proper fluorophore for labeling, we further investigated sensitivity of the system to different fluorescence probes. In this work, fluorescence marker with endothelial cells targeting was synthesized by cell staining technique using a 2-antibody procedure in which the primary antibody had affinity to the endothelial cells, whereas the secondary antibody was conjugated to a fluorescent probe and had affinity to the primary antibody. Based on formulation requirements we chose for our experiments following fluorescence probes: AlexaFlour 790, AlexaFluor 680, and CF660C. The sensitivity of the NIRF

system was compared in relation to these three fluorophores. Therefore, tube phantom was sequentially filled with all three dyes. Concentration was kept close to those expected after fluorescence labelling in the vessel (20 μg/ml). Then, NIRF signal from the tube phantom was recorded at a detector-to-target distance of 1.5 mm (**Figure 15**).
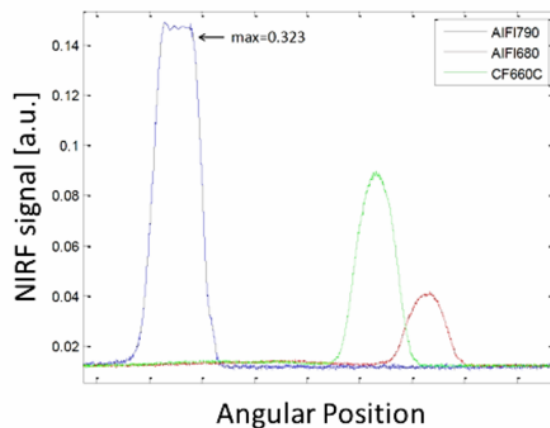
Figure 15. NIRF system sensitivity comparison. Maximum sensitivity was demonstrated for AlexaFluor 790 followed by CF660C and AlexaFluor 680.

The NIRF system demonstrated highest sensitivity for AlexaFluor 790. Three and 7.5 times lower sensitivity was measured for CF660C and AlexaFluor 680, respectively. Difference in sensitivity is mostly due to wavelength-dependent performance of system components, alignment parameters of the free-space optics combined with matching of corresponding optical filters. Based on these results, two fluorescent probes were identified to be used in the following studies: Alexa Fluor 790 and CF660C.

4.6 Validation of NIRF Imaging *Ex Vivo*

In the first study, we validated system for detection of the fluorescence distribution in the vessel *ex vivo.* NIRF contrast was created by means of CF660C and AlexaFluor 790 as a secondary antibody labels. Same as before, the NIRF system was optimized for maximum sensitivity for each fluorescent probe separately. Optical filters and excitation laser were chosen per excitation/emission wavelengths of fluorophores.

a) Fluorescence probes comparison.

In the **Experiment 1** we compared contrast of NIRF imaging when CF660C and AlexaFluor 790 are used as a secondary antibody. Therefore, rabbit iliac arteries were treated by angioplasty to induce damage of endothelial layer. Then, following euthanasia, arteries were explanted and immersed in anti-CD31 antibody according to PECAM-1 (Platelet Endothelial Cell Adhesion Molecule-1) protocol for immunostaining[78,79]. CD31 was expressed constitutively on the surface of adult and embryonic endothelial cells. Next, antibody labeling was performed with specific secondary antibody tagged with NIRF probe. Finally, arteries were dissected, cut into sections and imaged *ex vivo* using NIRF system. Fluorescence Microscopy (FM) was used to validate NIRF results. Staining and imaging was also performed on denuded and healthy aortas to quantify unspecific background level of the NIRF signal and calculate contrast.

Imaging of the native control, vessel with unspecific CF660/AlexaFluor 790 staining and CD31 specific CF660/AlexaFluor 790 staining is shown in **Figure 16**.
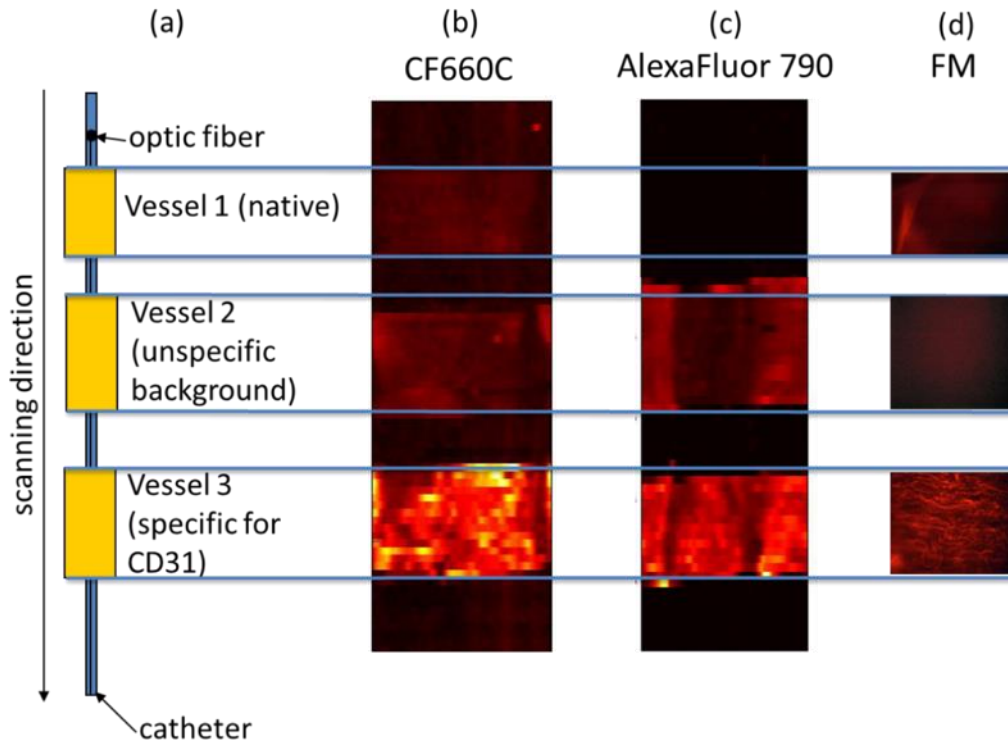
Figure 16. Comparison of CF660C and AlexaFluor 790 as a secondary antibody. Schematic view of the imaging configuration. (b) NIRF image of segments tagged with CF660C. (c) NIRF image of segments tagged with AlexaFluor 790. (d) Corresponding fluorescence microscopy slides.

As shown by NIRF imaging and confirmed by Fluorescence Microscopy (**Figure 16d**), NIRF signal was considerably stronger from a vessel segment with specific CD31 targeting compared to control segments for both probes. Probe tagged with AlexaFluor 790 (**Figure 16c**) demonstrated stronger fluorescence compared to CF660C (**Figure 16b**) probe. The difference was measured to be in order of magnitude. However, contrast, measured as ratio of mean signal between segments with specific and unspecific targeting, was computed to be 5.3dB and

3.5dB for CF660C and AlexaFluor 790 probes, respectively. SNR, measured as ratio of mean signal between segments with specific targeting and native vessel, was measured to be 5.2dB and 13dB for CF660C and AlexaFluor 790 probes, respectively.

Higher contrast from vessel segments with CF660C staining, despite higher SNR of the NIRF system for AlexaFluor 790, demonstrate that former probe has better specificity to the endothelial cells. Since the imaging contrast is of highest importance for reliable *in vivo* detection, the decision on the most appropriate probe for endothelial cells detection was based solely on this parameter. Therefore, the probe demonstrated better contrast was chosen as the preferred probe – CF660C.

b) Endothelium imaging ex vivo.

The **Experiment 2** was designed to test whether NIRF imaging can be used for distinguishing between healthy and damaged endothelial layer of the vessel. The hypothesis was that denuded arteries, in which the endothelium was damaged or removed, would show no or considerably less NIRF signal compared to native arteries with intact endothelium. To test the hypothesis, staining with the CF660C fluorescent probe was performed for both healthy and denuded rabbit aortas. Imaging of the controls and stained arteries was performed using the NIRF system and fluorescence microscope (**Figure 17**).
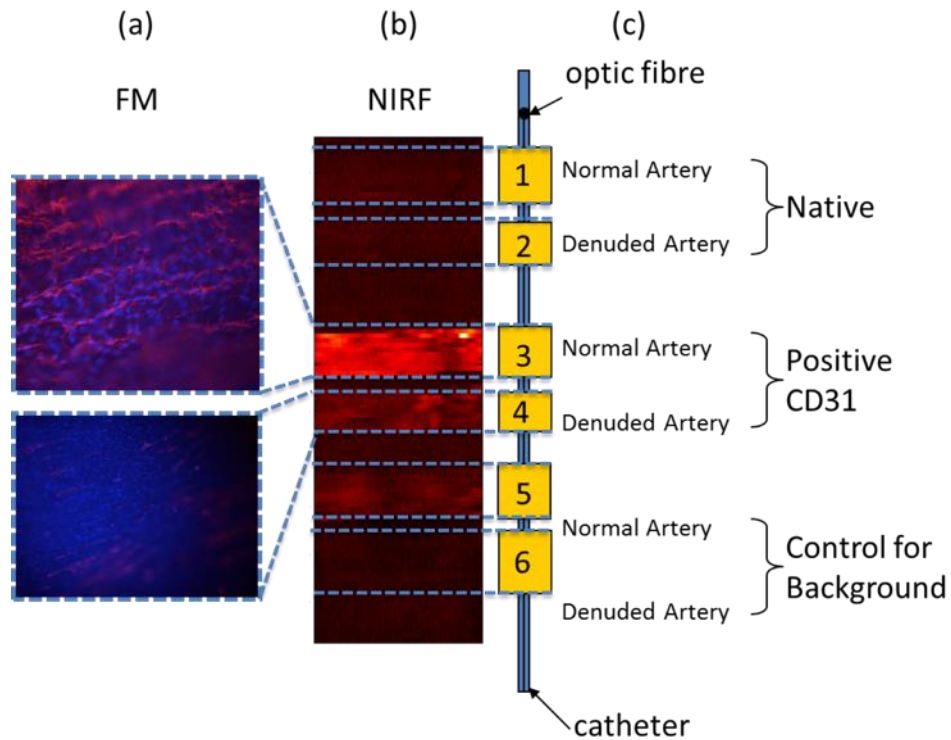
Figure 17. Change in NIRF signal Intensity after arterial denudation. Representative fluorescence microscopy slides. (b) NIRF image. (c) Schematic view of the imaging configuration.

Indeed, NIRF imaging showed the contrast to be 3dB (**Figure 17b**). This finding was also corroborated by a fluorescence microscopy performed on small sections of the aortas as shown in **Figure 17a**.

4.7 Discussion

In this framework, specific NIRF imaging was demonstrated *ex vivo*. We confirmed that engineered NIRF system can detect accumulation of the novel fluorescent marker and, thereby, differentiate areas of healthy vessel and areas with damaged endothelial layer. NIRF imaging was shown to be reliable, since all findings matched fluorescence microscopy results.

Our results suggest that this new approach can be used for detecting impaired endothelial function that occurs in vascular conditions associated with development of atherosclerosis as well as for assessing delayed re-endothelialization after stent implantation, which is known to be linked to stent thrombosis and adverse clinical outcomes[80].

However, *in vivo* application of this strategy requires further development. Primarily, to achieve quantitative NIRF readings through blood, correction for detector-vessel wall distance should be implemented. Therefore, accurately co-registered morphological readings using an ultrasound transducer should be performed simultaneously with molecular imaging. Meanwhile, the stand-alone NIRF catheter can be used to assess fluorescence activity in a semi-quantitative manner.

As a next step, the promising approach of endothelial imaging based on a NIRF system will be thoroughly investigated. Endothelial imaging will be performed in

stented blood vessels with the goal of determining whether the method can detect stent damage to the endothelium. Additionally, imaging will be performed in time series and will be validated using histology. Larger sample sizes will also be used to enable statistical analysis of the results. Quantitative imaging of fluorescence distribution will become possible with a dual-modality cNIRF-IVUS catheter. The next chapter of this work describes design, development and engineering of such a system.

5 cNIRF-IVUS System for Intravascular Imaging

This chapter will describe the first hybrid cNIRF-IVUS (c=corrected) imaging catheter system, which is capable of quantitative fluorescence and co-registered ultrasound imaging. cNIRF-IVUS was engineered by our group following the development of the NIRF imaging approach discussed in Chapter 4. Despite demonstrated promise, standalone NIRF is limited by two main features: first, NIRF by itself does not provide morphological information, which is a key aspect of current clinical interrogation and diagnosis; second, NIRF images do not represent the concentration of fluorophore in the wall of the blood vessel, but rather the amount of fluorescence light collected by the NIRF fiber. Nonetheless, the collected fluorescence signal is attenuated by the blood present in the vessel. Therefore, the NIRF images are affected by the relative geometry (distance) between the catheter and the vessel wall, which limits the accuracy and reliability of the method. To overcome the quantification challenges imposed by the intravascular geometry and presence of blood, NIRF imaging must be performed together with a precisely co-registered morphological visualization that reveals the vessel anatomy and the distance between the catheter and the luminal edge of the vessel at each angular position[30]. Additionally, imaging must be accompanied by a signal processing algorithm to correct NIRF signals for a distance-related attenuation and, thus, quantify fluorescence readings.

These requirements led to the development of NIRF-OCT[81] and NIRF-IVUS[29,66,82] intravascular hybrid catheters[83]. In case of NIRF-OCT, all-optical design allowed employment of the same optical fiber for both NIRF and OCT imaging and, thus, seamless integration into a coronary-size hybrid catheter with outer diameter as small as 0.8 mm[84]. On the other side, optical detection of morphology was limited to visualization only of superficial layers of artery wall and required blood flushing.

Herein, to enable quantitative NIRF detection through blood, we, first, integrated NIRF and IVUS detectors into a single catheter. In contrast to NIRF-OCT system, employment of ultrasound and high-sensitivity fluorescence detection allowed imaging without need for blood flushing. Second, we characterized imaging parameters of the dual system in phantom experiments. Third, IVUS-based distance correction algorithm was implemented. Contrary to previous studies[29,85], we showed that distance-correction algorithms calibrated on *ex vivo* data are not appropriate for correcting *in vivo* NIRF images. Therefore, we derived attenuation models exclusively from *in vivo* measurements. Finally, we validated the developed system and NIRF correction algorithm based on experiments with a vessel *ex vivo*.

5.1 Description of the cNIRF-IVUS Setup

Schematic view of the setup is presented in **Figure 18**. Hardware of the NIRF component in the cNIRF-IVUS catheter were identical to those in stand-alone NIRF. Briefly, the system employed a continuous wave (CW) laser source with central wavelength 750nm (B&W Tek Inc., Läbeck, Germany) for fluorescence excitation. The imaging catheter was based on an optical fiber with a NA= 0.22 and core size 200 μm. To guide laser illumination at a 90-degree angle from the fiber axis to the vessel wall, a 0.25mm micro prism (Precision Optics Corporation, Gardner, MA USA) was glued on the distal end of the fiber. Excitation and emission light shared the same path and were separated by a dichroic mirror (DM) with 765nm cut-off wavelength (AHF Analysentechnik AG, Täbingen, Germany) and three long pass filters with 780nm, 785nm and 800nm cut-off wavelengths. Then, fluorescence photons were detected by a photomultiplier tube (PMT) (Model H5783-20, Hamamatsu Photonics, Shizuoka Pref., Japan).

NIRF detector was integrated with an ultrasound transducer. Both were aligned so that angular and longitudinal offset between optical and ultrasonic beams was 6.8 grad and 90 μm, respectively. In parallel with NIRF detection, transducer emitted short ultrasound pulses and detected reflected from the vessel wall echo signals. Therefore, short negative voltage impulses with repetition rate 10 kHz were generated by pulser-receiver (Olympus 5073PR, Hamburg, Germany)

and sent to the transducer. Received echoes were amplified using 39 dB amplifier. Finally, NIRF and IVUS data was digitized at sampling frequency 200 MSample/sec using two channel high-resolution oscilloscope/digitizer (NI PCI-5124, Munich, Germany).

Hybrid cNIRF-IVUS catheter was housed within a transparent polymer sheath which had a radiopaque marker on the distal end for angiographic guidance. For ease of use, distal end of the sheath was equipped with a port for a monorail guide-wire. cNIRF-IVUS console was assembled on a transportable table to allow use in an operation room (**Figure 18b, c**). Hybrid sensor was automatically pulled back and rotated inside the sheath using mechanical stages (Orienal Motor co Ltd, model EZ Limo and VEXTA). Rotation speed was up to 180 rotations per minute (rpm).
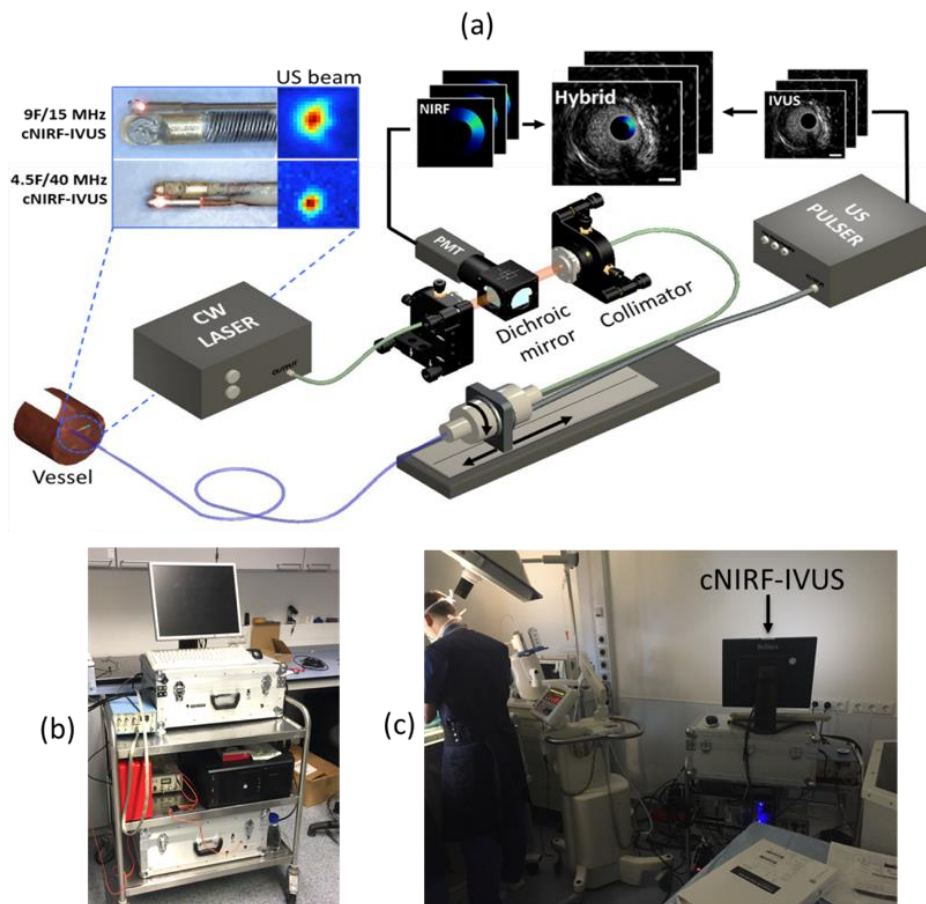
Figure 18. cNIRF-IVUS imaging system. (a) Stand alone NIRF system was extended with structural imaging by means of IVUS transducer. (b) cNIRF-IVUS console for preclinical investigations. (c) cNIRF-IVUS system installed in an operation room.

Data acquisition and pullback were controlled by program written in LABVIEW environment (NI, Munich, Germany). User-friendly interface allowed operator to set-up parameters such as pullback step and length, speed of rotation, sampling frequency. NIRF and US signals were displayed in real-time for visual control.

Two models of the hybrid catheter were engineered. First was used to image bigger (peripheral) lumens (diameter > 5 mm). It employed a 15 MHz IVUS transducer and was housed within a fluorinated ethylene propylene (FEP)

transparent tube (Zeus, Orangeburg, SC USA) with OD = 9F (3 mm). Reflection of the ultrasound energy from the water-FEP interface was measured to be 30-50% each way. To avoid such a significant loss during measurements, detector was pushed out of the tube when catheter was positioned in the region of interest. This way pullback was performed with the fiber tip and ultrasound transducer exposed to surrounding media (blood or saline). Due to short pullback length and big diameter of the lumen, risk to damage a vessel was considered minimal.

Second model of the dual-modality cNIRF-IVUS catheter was used to image smaller lumens (coronary arteries; diameter < 5mm) with high resolution. It utilized a 40 MHz IVUS transducer. Catheter was housed within a tube with OD = 4.5F (1.5 mm). Distal end of the tube was sealed and tube was filled with distilled water for ultrasound coupling. Owing to close acoustic impedances of LDPE and water (1.79 MRayls and 1.48 MRayls, respectively) attenuation of ultrasound energy on water-LDPE interface was measured to be 5-10% each way. This allowed us to image from within the tube without direct contact between detector and surrounding media.
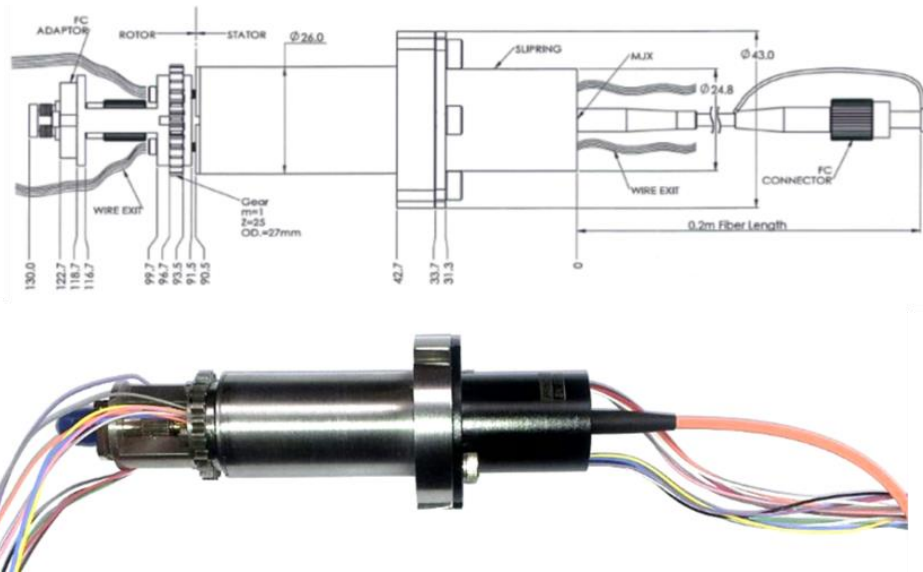
Figure 19. Schematics and photograph of the NIRF-IVUS rotary joint.

Custom hybrid rotary joint (Princetel Inc., Hamilton Township, NJ USA) was built to interface rotating catheter and stationary part of the system (**Figure 19**). It offered (i) direct fiber-to-fiber light coupling through precise alignment between the stationary and rotating fibers; (ii) transmission and reception of the ultrasound readouts by coupling electrical signals through a concentric slip ring built around the fiber. Both ways pass insertion losses for US signals caused by rotary joint were measured to be 2 dB and 5 dB at central frequency of 15 MHz and 40 MHz, respectively. Single pass optical loss was measured to be 3.7 dB.

5.2 Characterization of Ultrasound Resolutions

Full characterization of NIRF imaging paramaters is presented in **Chapter 4.5**. Briefly, system can resolve two fluorescent targets at lateral distances >0.46mm at typical imaging range 0.5-1.5mm. Sensitivity allows detection of 500 nM of AlexaFluor 750 at a fiber-to-target distances up to 2.2 mm in *ex vivo* blood.

Ultrasound resolution of the cNIRF-IVUS catheter was determined by transducers geometry and central frequency. To find ultrasound resolution, copper string 100 μm in diameter was imaged using 9F/15MHz and 4.5F/40MHz catheters at different distances. Full width at half maximum of the signals was then calculated and plotted versus catheter-target distance as shown in **Figure 20**.
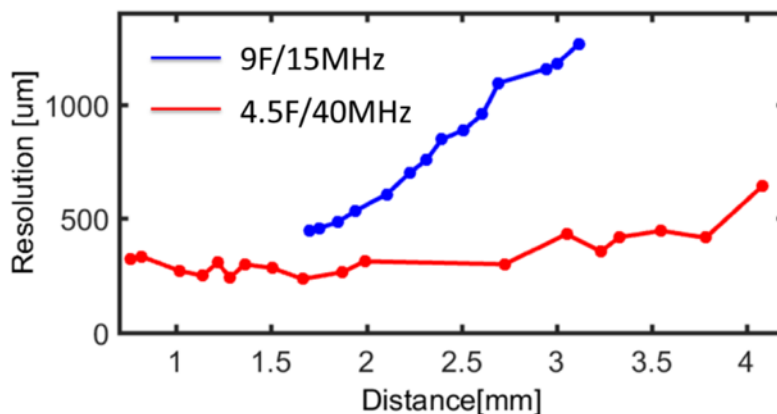

Figure 20. Ultrasound resolution of 4.5F/40MHz and 9F/15MHz cNIRF-IVUS catheters. Due to higher central frequency, 4.5F/40MHz catheter demonstrated higher resolution compared to 9F/15MHz catheter.

As expected, ultrasound resolution degraded with distance for both 4.5F/40MHz and 9F/15MHz catheters. However, 40 MHz model demonstrated less degradation in whole range of measurements. At imaging distance of 2 mm, 40 MHz model demonstrated twice better resolution compared to 15 MHz model: 300 µm and 533 µm, respectively, which corresponds to angular resolutions of 8º and 16º. Axial resolutions were not affected by distance and were determined only by central frequencies. They were measured to be 150 µm and 240 µm for 40 MHz and 15 MHz modification of the catheter, respectively, which is comparable with resolutions of commercially available IVUS systems.

Additionally to estimation of resolution from FWHM of the signal, we measured lateral ultrasound resolution of the 4.5F/40MHz catheter as minimal distance at which two targets are resolved. For this experiment, we build a cross-phantom. It was constructed from two crossed polyethylene tubes 1 mm in diameter visible in ultrasound. Phantom was placed inside a water bath and scanned using cNIRF-IVUS catheter. IVUS lateral resolutions was measured as a minimal distance at which two tubes were resolved based on cross sectional images (**Figure 21a**). Measured this way lateral resolution was measured to be 370 µm.
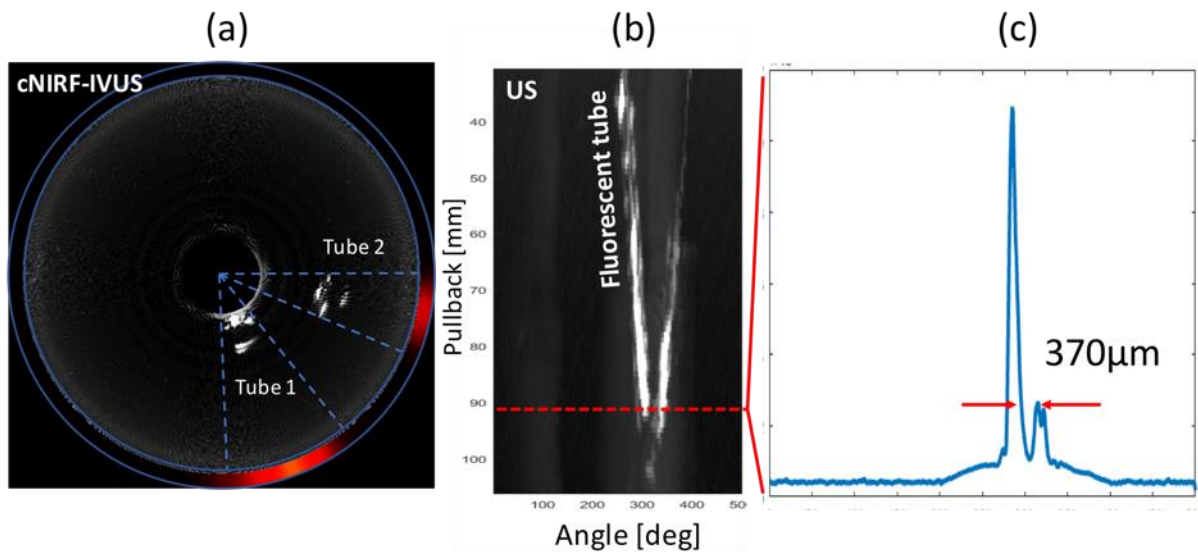
Figure 21. Experimental measurement of ultrasound resolution. (a) Representative cNIRF-IVUS cross sectional image of the cross phantom. (b) Maximum intensity projection of ultrasound image showing cross phantom. (c) Ultrasound A-line at pullback position 92mm where two tube are still resolved.

Figure 22 shows comparison between abdominal rabbit aorta imaged with 9F/15MHz and 4.5F/40MHz hybrid catheters. As expected, higher central frequency results in visualization of finer morphological details.
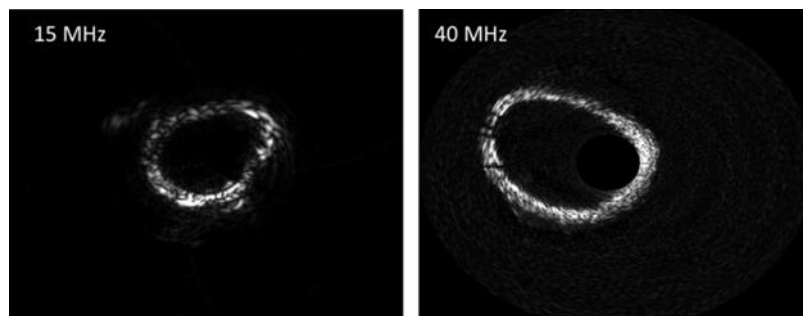

Figure 22. Representative image of the vessel using 9F/15MHz and 4.5F/40MHz catheters. Higher central ultrasound frequency of the 4.5F/40MHz catheter allows imaging with finer details compared to 9F/15MHz catheter.

We further summarized imaging characteristics of the developed cNIRF-IVUS catheters into a comprehensive table shown below.

Table 2. Imaging characteristics of the cNIRF-IVUS catheters.

		Resolution	Penetration depth	Through blood imaging
IVUS	40MHz	Lateral=300µm; Axial=150µm	~10mm	YES
	15MHz	Lateral=533µm; Axial=240µm	~20mm	
NIRF	In saline	670µm	4mm	YES
	In blood	~ 800µm	2mm	

5.3 Reconstruction of NIRF-IVUS Data

Collected NIRF and US data was processed offline using MATLAB (R2013b, The MathWorks, Inc.) and ImageJ (v1.45s, National Institutes of Health, USA) software. The reconstruction algorithm for the hybrid images before distance correction is illustrated by **Figure 23**. First, data was down-sampled by averaging so that every cross-sectional ultrasound B-scan was composed of approximately 400 ultrasound A-lines. Second, every ultrasound A-line was associated with a corresponding NIRF value. Therefore, angular and axial offsets between US and NIRF beams were taken into account. Cross sectional ultrasound images in polar coordinates were then formed from ultrasound A-lines and rendered in gray scale. NIRF signals were overlaid on the origin of each ultrasound image using black-blue-green color scheme. Finally, the resulting hybrid image was converted into Cartesian coordinates.
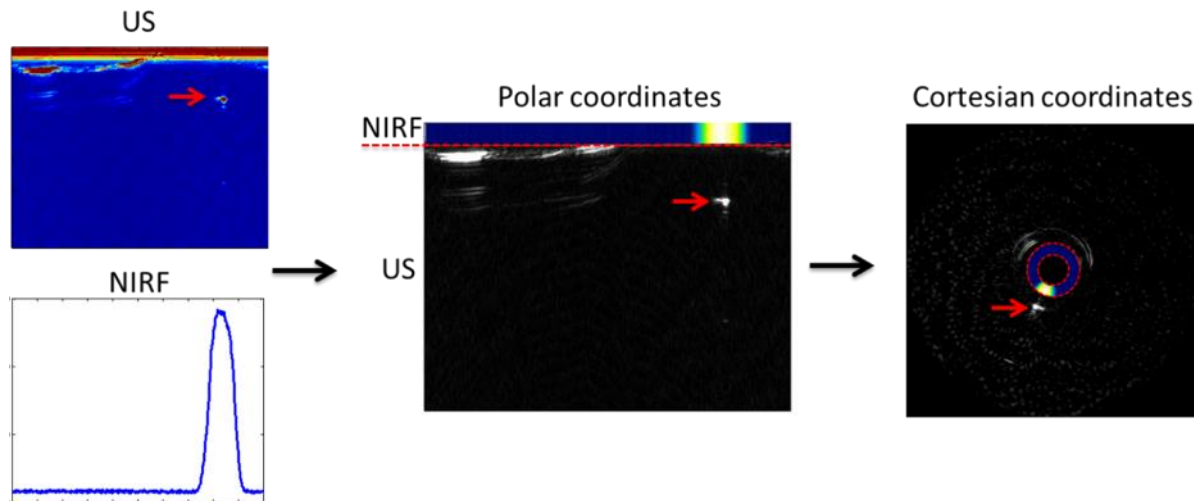
Figure 23. Post-processing algorithm for cNIRF-IVUS data. After down-sampling NIRF and IVUS images are overlaid in Polar coordinates and then converted to Cartesian.

To show fluorescence signal obtained over the entire pullback, NIRF signals were also converted into two-dimensional image where long axis represented pullback position and short axis corresponded to angular position of the catheter. More details on reconstruction of NIRF images are presented in **Chapter 4.3**.

5.4 Development of the NIRF Correction Algorithm

For attenuation correction of NIRF data we first assumed that detected fluorescence is generated in the superficial layer of the blood-vessel wall. Such an assumption is based on the fact that fluorescence dyes accumulate close to the inner surface of the vessel wall[76,86]. It was also shown by Jaffer at al.[87] that plaque tissue is less likely to attenuate NIRF signals. Thus, it could be considered

that detected fluoresce experiences attenuation only in blood and could be described by the equation[88,89]

$$P = P_0 CR/\alpha(r) \qquad (25)$$

where P is the amplitude of the detected fluorescence signal, P_0 is the illumination at the distal end of the fiber, C is the unknown concentration of the fluorochrome within detected volume, R is a constant related to optical properties of the imaged fluorescent probe such as absorption coefficient and quantum yield, and $\alpha(r)$ is the value of the distance-dependent attenuation function. According to **Eq.25**, the true fluorophore concentration can be found by dividing the measured signal by $P_0 R/\alpha(r)$:

$$C = \frac{P\alpha(r)}{P_0 R}. \qquad (26)$$

The parameter $P_0 R$ scales the concentration linearly, if no quenching occurs. In practice, calibration of R to the specific probe imaged is required. Otherwise, the measured concentration C may only be represented in arbitrary units. Here. such a calibration was performed by relating the collected NIRF signal from a fluorescence phantom to the known concentrations and distances in controlled measurements.

Noise in the detected signal P might be amplified by the correction formula **Eq.26** and lead to spurious signals. Therefore, the distance correction was regularized

to handle noise. We introduced a regularization function β that suppresses any signal below the noise level to minimize their subsequent amplification:

$$C = P\beta\alpha(r)/P_0 R \qquad (28)$$

β is a function of the detected signal P and described by equation

$$
\begin{cases}
\beta = 32\left(\dfrac{P}{P + P_{noise}} - \dfrac{1}{2}\right)^2, & if\ P \leq 3P_{noise} \\[4mm]
\beta = 1 - 32\left(\dfrac{P}{P + P_{noise}} - \dfrac{1}{2}\right)^2, & if\ P > 3P_{noise}
\end{cases}
\qquad (29)
$$

5.5 Difference Between Blood Attenuation *Ex Vivo* and *In Vivo*

We experimentally found that blood measured *in vivo* exhibits less light attenuation compared to *ex vivo* NIRF detection, possibly due to different oxygenation status and blood flow[40,51]. Consequently, NIRF correction could not be based on *ex vivo* values found in the literature. Instead we developed a novel algorithm based on Twersky model for transmission measurements[33] (see **Chapter 3.1.4**) calibrated in *in vivo* settings. The algorithm operates on the fluorescent measurement obtained and corrects it for catheter-vessel-wall distance and blood attenuation to retrieve the true fluorescence intensity on the inner surface of the arterial wall. Furthermore, we showed that cNIRF-IVUS could dynamically observe blood attenuation changes depending on hematocrit that can further optimize system operation under varying attenuation conditions.

The algorithm is only applicable to the hybrid system, whereby co-registered measurements of fluorescence intensity (by NIRF) and of distance (by IVUS) are introduced in a global minimization problem, which solves for blood attenuation.

Ex vivo cNIRF-IVUS measurements of blood attenuation. To determine the distance-attenuation function $\alpha(r)$ we employed the setup shown in **Figure 24a**. cNIRF-IVUS pullback was performed at 25º angle to a tube filled with AlexaFluor 750. By combining distance measurements with NIRF intensity values, the $\alpha(r)$ was calculated based on fitting the measurements to the Twersky model for saline (blue dots in **Figure 24e**) and swine blood (green dots in **Figure 24e**) *ex vivo.*

In vivo cNIRF-IVUS measurements of blood attenuation. For determining the distance-attenuation function $\alpha(r)$ *in vivo*, we also analyzed AlexaFluor 750 intensities obtained from the intravascular measurements in living swine after injection of the AlexaFluor 750 directly into the vessel wall, as detailed in **Chapter 6.1**. The *in vivo* results are shown by red dots in **Figure 24e**. We observed that NIR light attenuation by *in vivo* blood was significantly less than by *ex vivo* blood. This finding could be related to differential oxygenation levels of blood[40,42], the presence of flow[40,44,46], and/or the effect of absorption flattening[49,50]. The Twersky model fits the curve corresponding to *in vivo* blood measurements with $R^2 = 0.98$ with parameters *q*=0.32 and *B*=24.9.

In this work, we assumed blood absorption to be consistent throughout the arterial circulation. One potential limitation to this approach is that the optical properties of blood are influenced by the blood velocity variations present in different arterial beds, with slower blood velocity resulting in higher light absorption. According to published data[40], blood flow-based variations in optical attenuation are relatively small and do not exceed 12%. Therefore, the computed distance-attenuation function *α(r)* is anticipated to reasonably correct *in vivo* NIRF signals acquired from both the carotid and coronary arteries.

To demonstrate the ability to use distance-based correction of fluorescence images we performed an independent 15 mm cNIRF-IVUS pullback using the setup in **Figure 24a**. The resulted NIRF image is shown in **Figure 24c**. Weighting per **Eq.26** was applied to recorded NIRF signals. The distance-attenuation model $\alpha(r)$ measured in saline was used for correction. As expected, NIRF intensities were recovered, revealing constant concentration of the fluorophore in the tube (**Figure 24d**), compared to the raw data erroneously showing a varying concentration of fluorophore.
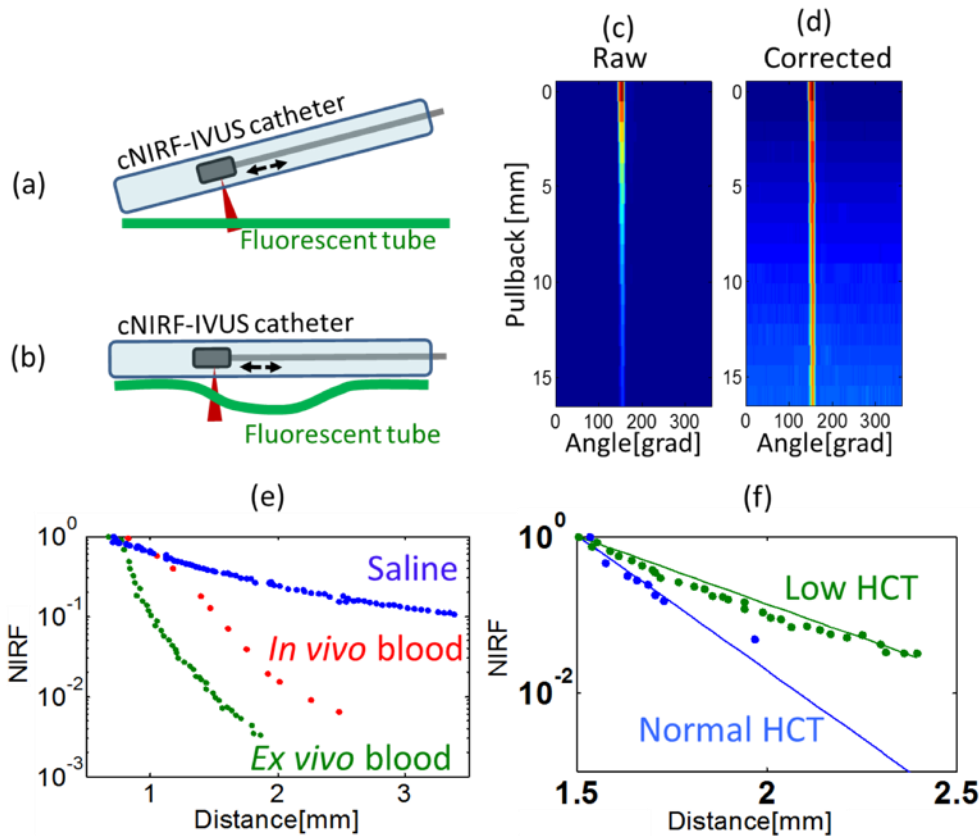
Figure 24. Measurements and validation of distance attenuation model α(r). (a) Setup arrangement for measurement of $\alpha(r)$ in saline and ex vivo blood. (b) Setup arrangement for in vivo validation of cNIRF-IVUS ability to resolve attenuation changes in blood using a fluorescent tube phantom. (c) NIRF signal from a tube with AlexaFluor 750 detected over increasing catheter-target distance before (c) and after (d) distance correction. (e) Distance attenuation model $\alpha(r)$ measured in saline (blue), in vivo blood (red), and ex vivo blood (green). (f) Light attenuation due to blood with normal (blue) and low (green) level of HCT measured in vivo with cNIRF-IVUS. Lines represent fits to Twersky model.

The results shown in **Figure 24c, d** confirmed the ability to perform attenuation correction of fluorescence intensities given a known attenuation function $\alpha(r)$. However, it was unknown if the cNIRF-IVUS system could be employed to dynamically characterize blood attenuation during an experimental measurement. For this reason, we investigated whether cNIRF-IVUS could be sensitive to hematocrit changes, by building the phantom shown in **Figure 24b**. i.e. a flexible fluorescent tube containing AlexaFluor 750 was placed next to the

catheter. The overall diameter of the tube – catheter phantom was 2.6 mm, i.e. small enough to insert it to the aorta of living pig through a 9F introducer. *In vivo* measurements of the phantom arrangement were performed under regular *htc* levels (blue dots **Figure 24f**) and following dilution of *htc* to 0.25, using saline perfusion (green dots in **Figure 24f**), confirmed by drawing blood samples. Lines in **Figure 24f** represent fits to the Twersky model.

Phantom measurements confirmed the ability of the cNIRF-IVUS system to track attenuation changes of blood, but required phantom measurements of known fluorophores. To further interrogate whether blood-attenuation changes would be possible *in vivo*, during intravascular measurements we analyzed cNIRF-IVUS intravascular imaging data obtained *in vivo* from rabbit measurements. **Figure 25a** plots fluorescence intensity values in relation to the catheter–vessel wall distance obtained *in vivo* from abdominal aorta from an intact area that contained no lesions. We discovered a low-frequency varying fluorescence intensity component (**Figure 25a**) which inversely correlated with the catheter–vessel wall distance (**Figure 25c**). This signal is attributed to the background wall fluorescence and could be employed to dynamically estimate blood attenuation measurements *in vivo*. **Figure 25a** and **Figure 25b** show representative examples of fluorescence distribution in a healthy vessel. **Figure 25c** displays a cNIRF-IVUS cross section in polar coordinates where the vessel wall and the catheter are

outlined by red and magenta lines, respectively. By plotting the fluorescence intensity values normalized for beam size at a corresponding distance, we could obtain the same attenuation function $\alpha(r)$ as from *in vivo* phantom measurement shown in **Figure 24**. This finding signifies the cNIRF-IVUS ability to retrieve the attenuation function $\alpha(r)$ *in vivo*, which can be employed to dynamically monitor against changes of blood attenuation, e.g. due to hematocrit variations. The suggested herein dynamic observations of blood attenuation can be applicable in cases of efficient clearance of the fluorophore from the blood circulation. This practice is consistent with the administration of fluorescent agents targeting biological biomarkers, since it also allows time for efficient targeting and maximizes imaging contrast as well.
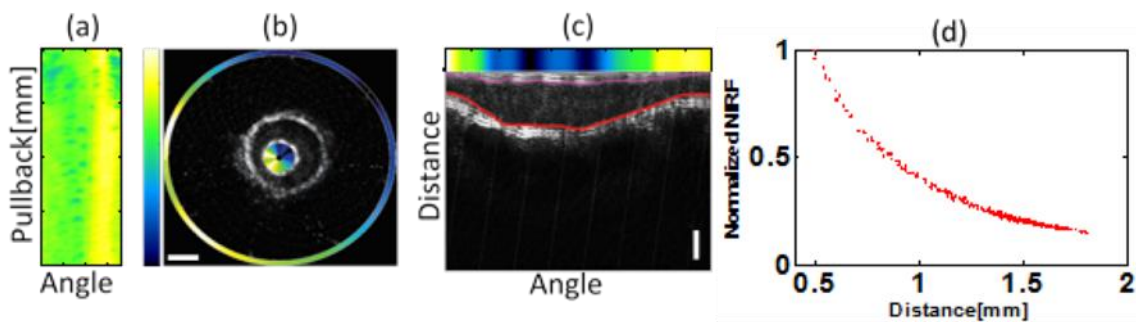

Figure 25. Attenuation function derived from in vivo measurements in abdominal aorta of a rabbit without a priori knowledge of blood parameters. (a) NIRF pullback in a healthy vessel after systematic injection of fluorescence agent. Low-frequency component correlates with catheter position within a vessel. (b) Representative cNIRF-IVUS cross-section of the healthy vessel. (c) cNIRF-IVUS cross-sections converted to Cartesian coordinates were used to calculate a thickness of blood through which fluorescence was detected. Red and magenta lines outline lumen. (d) NIRF signal normalized for beam size as a function of catheter-to-vessel wall distance. All scale bars 1mm.

5.6 Validation of the NIRF Correction Algorithm

To validate the system and correction algorithm in experimental conditions reflective of coronary arterial dimensions, the hybrid catheter was placed inside an abdominal rabbit aorta *ex vivo* (diameter 4mm). Next, an NIR fluorophore (AlexaFluor750, 0.15 ml volume, concentration 0.5 mg/ml) was locally injected into the wall of aorta to simulate fluorophore accumulation in the arterial wall. The same region of the vessel was scanned 3 times with the 9F/15MHz cNIRF-IVUS catheter. Between pullbacks, the cNIRF-IVUS catheter was manually re-advanced into the same starting position but placed in a different intraluminal position for each pullback (position 1-3 in **Figure 26**). Subsequently, the NIRF signals were corrected for distance variations per correction algorithm described in **Chapter 5.4**.

Figure 26a show representative cross-sectional hybrid cNIRF-IVUS images of the vessel. A colored circular ring in the center shows NIRF signal before and after the correction. The raw and corrected NIRF signals obtained over whole pullbacks are displayed next to the hybrid cross sectional images (**Figure 26b**).
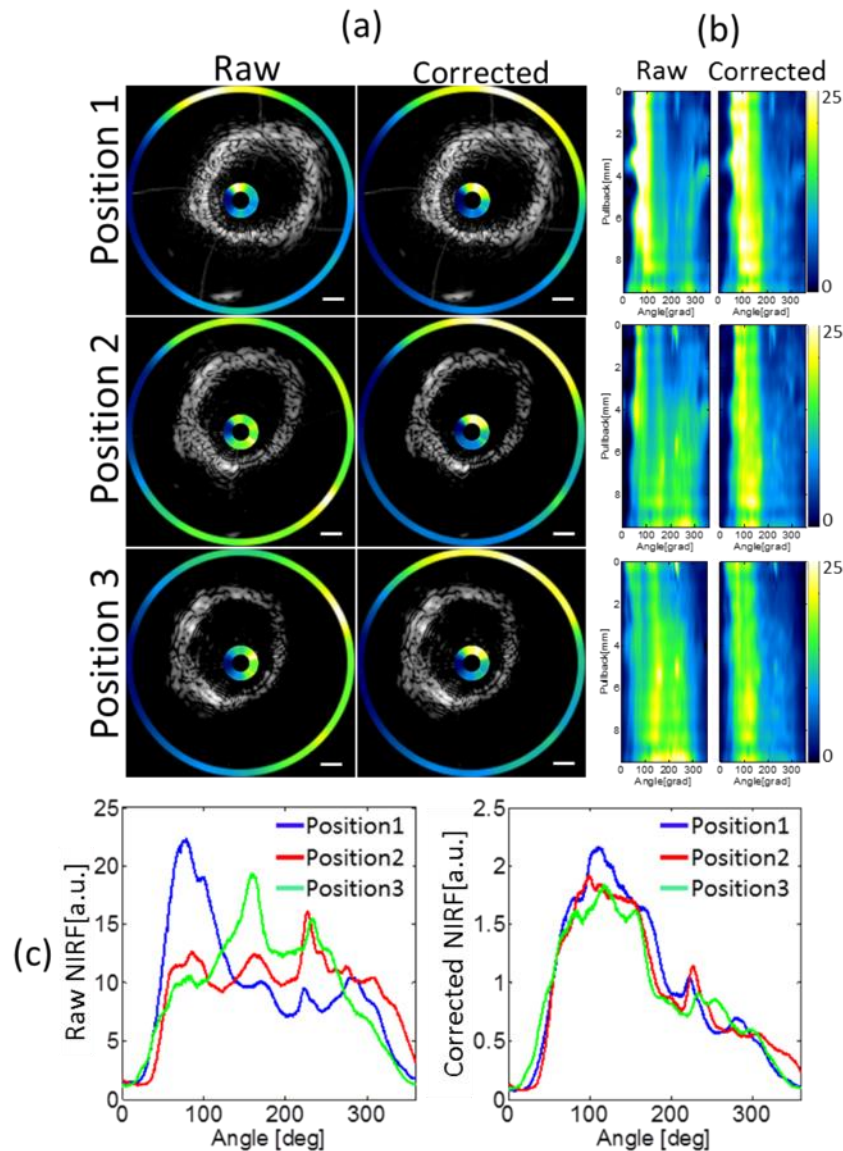
Figure 26. Results of ex vivo imaging experiments in the abdominal aorta of a rabbit following AF750 NIR fluorophore injected into the artery wall. (a) Three imaging sessions of the same region of the vessel were performed with catheter placed in different intraluminal positions. Representative ultrasound image of the vessel cross section obtained from each position is presented in black and white colors. Each colored circular ring represents corresponding raw NIRF or corrected NIRF signals, and are depicted on the interior of the IVUS catheter, as well as externally around the vessel wall. (b) Representation of the raw and corrected NIRF two-dimensional images obtained in different intraluminal positions. (c) Comparison between raw and corrected 1D NIRF signals. All scale bars 1mm.

A visual comparison of the corrected NIRF images **in Figure 26b** showed greater

consistency compared to uncorrected images. For example, the raw NIRF images

shown in **Figure 26a** for positions 2 and 3 manifest a higher NIRF signals at 4-6

o'clock owing to less blood volume between the catheter and the arterial wall NIR fluorophores in these angles. In comparison, the raw NIRF image in position 1, in which the catheter is located further from the artery wall at 4-6 o'clock, shows a lower uncorrected NIRF intensity at these angles. In the corrected images, the signal at 4-6 o'clock is consistent among all three positions. The effect of the correction on the consistency of the NIRF signals may be also appreciated from their 1D plots shown in **Figure 26c**.

To quantitatively analyze reproducibility of corrected NIRF data, two parameters were computed for images obtained in different intraluminal positions: a) correlation coefficient between 2D NIRF images; b) relative standard deviation (RSD) between energies of the fluorescence signals. Energy of each signal was calculated as followed:

$$E = \sum_i m_i^2, \tag{30}$$

where m_i is intensity of the pixel, and i is a number of pixels in the NIRF image. All reproducibility analysis parameters are shown in **Table 3**.

a.

Raw images correlation

	Position 2	Position 3
Position 1	0.6924	0.5283
Position 3	0.7725	

Corrected images correlation

	Position 2	Position 3
Position 1	0.9483	0.9054
Position 3	0.9113	

b.

	Energy of the Raw signal	Energy of the Corrected signal
Position 1	2.87E+13	3.48E+05
Position 2	2.12E+13	2.68E+05
Position 3	2.31E+13	2.35E+05

| **RSD ,%** | **16.08** | **20.47** |

Table 3. Reproducibility analyses of the ex vivo measurements for similar catheter positions. (a) Correlation coefficients between raw and corrected NIRF images presented in Figure 26. (b) RSD calculation for raw and corrected NIRF images.

Although the RSD slightly increased (from 16.08% to 20.47%), distance correction resulted in a 26% higher correlation between NIRF images (average correlation 66% before correction, 92% after correction). This demonstrates a beneficial effect of the correction on the reliability of NIRF imaging.

To simulate a scenario where, instead of a small catheter movement, significant repositioning within the vessel occurs, the catheter was placed in top-right and bottom-center positions (**Figure 27**).
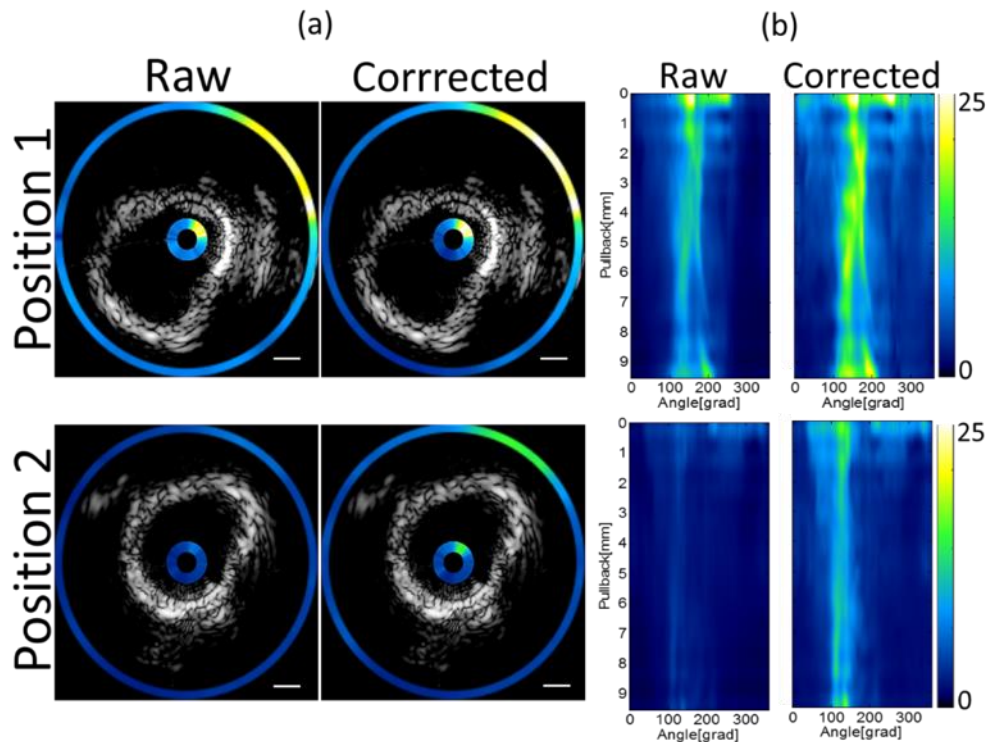
Figure 27. Results of ex vivo measurements in abdominal rabbit aorta with AF750 injected into the vessel wall after significant repositioning of the catheter. (a) Two imaging sessions of the same region of the vessel were performed with catheter placed in different intraluminal positions: top right (Position 1) and bottom-center (Position 2). Representative examples of the ultrasound images obtained from different positions are presented in black and white colors. Colored circular rings represent corresponding NIRF signal, and are depicted on the interior of the IVUS catheter, as well as externally around the vessel wall. (b) Raw and corrected NIRF images obtained over whole pullback in Position 1 and Position 2, respectively. All scale bars 1mm.

In cases of eccentric catheter position, the maximum amplitude of the NIRF signal in **Figure 27** position 1 was higher compared to the maximum amplitude of the signal in position 2. Nevertheless, the NIRF signals were normalized after applying the distance correction process. Reproducibility analysis showed that after correction RSD was reduced to half: from 100.29% to 57.12% (**Table 2**).

	Energy of the Raw signal	Energy of the Corrected signal
Position 1	7.79E+12	3.66E+04
Position 2	1.33E+12	1.56E+04

RSD, %	100.29	57.12

Table 4. Reproducibility analyses of the ex vivo measurements for eccentric catheter positions.

It is important to note that distance correction algorithm did not result in perfect co-registration due to errors in detector-to-target distance measurements. It should be considered that the more complicated morphology of the vessel compared to phantom used for distance-attenuation function measurement introduces errors.

6 Preclinical Validation of the cNIRF-IVUS System

After successful *ex vivo* validation of the developed system and correction algorithm, we proceed to pre-clinical *in vivo* tests. Performance of the 4.5F/40MHz and 9F/15MHz catheters was investigated in several clinical-relevant scenarios using rabbit and swine models.

6.1 *In vivo* Assessment of Reproducibility

To investigate whether the developed catheters can obtain images through *in vivo* blood in reproducible manner, male Yorkshire pigs (40-47 kg, N=2) were imaged using the 4.5F/40MHz cNIRF-IVUS catheter. Imaging was performed in the carotid artery *in vivo* (similar diameter as human coronary arteries, therefore suitable for this experiment with the 40 MHz, 1.5mm diameter catheter) based on MGH IACUC Protocol #2012N000066. Pigs were anesthetized using telazol (4.4 mg/kg) and xylazine (2.2 mg/kg), followed by isoflurane (Patterson Veterinary Supply, Devens, MA, USA). The ECG, oxygen saturation and invasive arterial blood pressure were monitored throughout the procedure. After surgical exposure of the carotid artery, a 6 French sheath was placed into the distal carotid artery. Then, a NIR fluorophore (AlexaFluor 750, 0.2 ml, concentration 50 μM) was injected into the outer wall of the proximal carotid artery. The 4.5F/40MHz cNIRF-IVUS catheter was inserted through the sheath into the

proximal carotid artery, and three sequential cNIRF-IVUS pullbacks were performed. Between pullbacks, the catheter was re-advanced to the same starting position using x-ray fluoroscopic guidance. Following *in vivo* imaging and euthanasia, the artery was harvested and blood flushed. Finally, FRI was performed *ex vivo* for validation purposes.
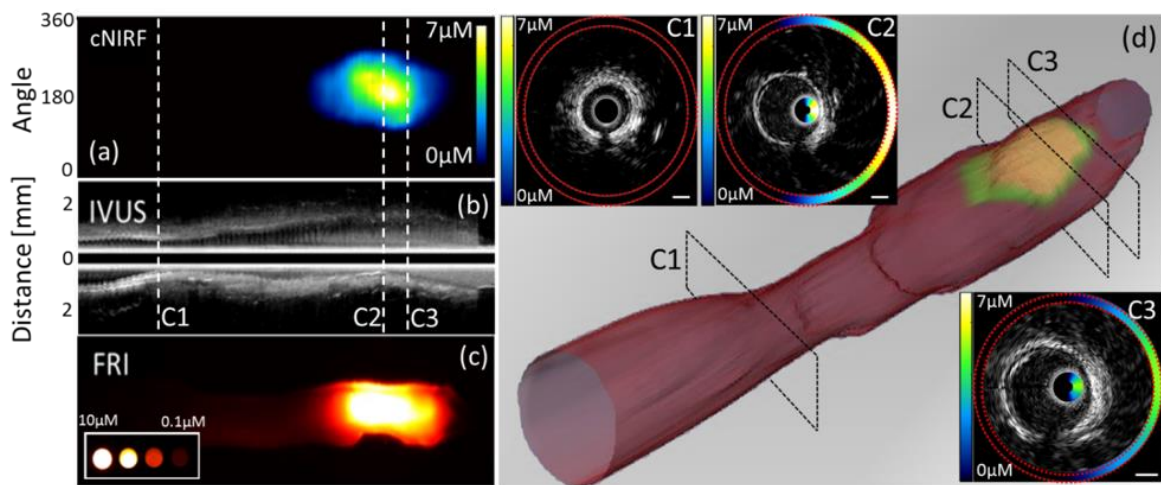

Figure 28. In vivo assessment of cNIRF-IVUS reproducibility. Images (a), (b), and (c) show a cNIRF image, the corresponding longitudinal IVUS image, and the FRI of the, respectively. (d) A three-dimensional representation of the lumen and arterial wall NIR fluorescence signal rendered based on the in vivo cNIRF-IVUS measurement. Inset figures C1, C2 and C3 show representative examples of the cross-sectional cNIRF-IVUS images corresponding to pull back positions C1 C2 and C3 in (a), (b) and (d). The cNIRF signal in C1, C2, and C3 inset axial images is fused onto the interior and exterior of the IVUS catheter.

Figure 28a and **b** represent cNIRF and longitudinal IVUS images of the artery *in vivo*. While not evident on IVUS, point of the fluorophore injection is clearly identified by co-registered NIRF modality. A 3D-rendered image of the lumen and fluorescence activity, shown in **Figure 28d** was generated from cNIRF-IVUS data. Insertion C1, C2 and C3 show representative examples of the cross-

sectional hybrid images corresponding to the pullback positions C1, C2 and C3 in

(a), (b) and (d). Good visual correlation of the cNIRF image was observed when

compared to FRI shown in **Figure 28c**. Absolute value of the maximum

fluorophore concentration detected by cNIRF-IVUS catheter (7 µM) agrees with

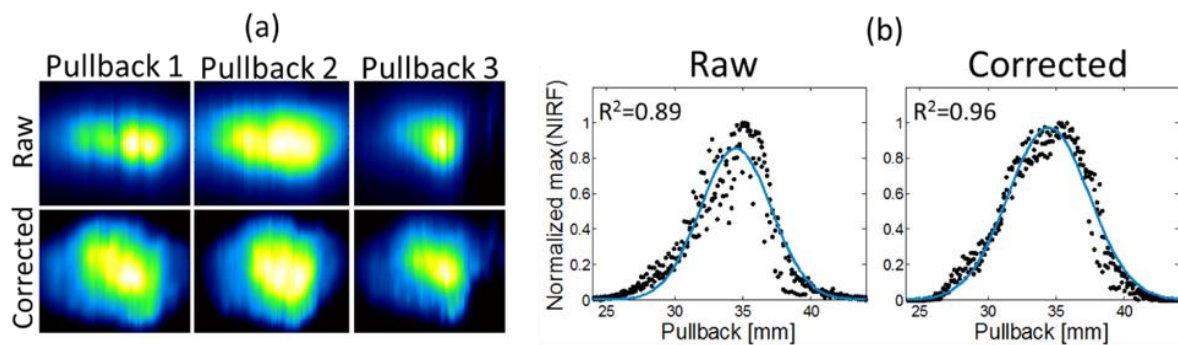one measured by FRI (10 µM) within 30% accuracy.

Figure 29. Reliability assessment of cNIRF-IVUS imaging in vivo. (a) Serial imaging of the same region of the vessel (top row) showed that NIRF images are affected by variable intraluminal catheter location and by heartbeat and breathing motions. However, NIRF distance correction substantially improved the reproducibility of the NIRF image and lessened motion artifacts (bottom row). (b) Corrected NIRF pullback images achieved better imaging accuracy. The maximum of the NIRF signal for every pullback position from three pullbacks is shown with black dots, blue line shows average distribution.

The NIRF images from all three pullbacks before and after distance correction

are shown in **Figure 29a**. Although the same region of the vessel was scanned,

significant inconsistency was observed among the uncorrected NIRF images

(**Figure 29a** top row). This finding can be attributed to the varying intraluminal

catheter position after re-advancements and variations in the catheter position

inside the artery due to blood flow and respiratory motion. Distance correction

of the NIRF signals, based on the exactly co-registered IVUS image depicting the

catheter position, and substantially improved the consistency of the NIRF results (**Figure 29a** bottom row) and congruence with the *ex vivo* image. The positive effect of the correction is also evident by observing the agreement of relative intensity of the NIRF signals between pullbacks (**Figure 29b**, black dots). Elevated dispersion of data points around the average distribution (blue line, R^2=0.89) in the case of raw NIRF signals shows a negative effect (image degradation) from rapid motions during pullback. Greater agreement of the NIRF signals from all three pullbacks was achieved by distance-correction (R^2=0.96).

In this experiment, we showed, that cNIRF-IVUS system provides reproducible morphological and co-registered molecular images through flowing *in vivo* blood. Distance correction algorithm was demonstrated to compensate for blood attenuation resulting in more reliable NIRF readings. Absolute value of fluorophore concentration measured *in vivo* are shown to be accurate.

6.2 cNIRF-IVUS Detection of ICG

Ability to detect ICG *in vivo* is critical parameter for translatable imaging system. Percutaneous transluminal angioplasty, a mainstay treatment of clinically obstructive atherosclerosis, can induce vascular injury that may not be readily visualized with conventional imaging methods such as standalone IVUS. Hence, we chose this model to investigated whether cNIRF-IVUS could detect ICG

deposition in peripheral swine arteries *in vivo*. Therefore, angioplasty-induced vascular injury was imaged *in vivo* in mechanically injured swine peripheral arteries (N=3). The distal femoral arteries (average diameter 3.1 mm based on *in vivo* IVUS measurements) of two animals were interrogated with the 4.5F/40MHz catheter. To explore the performance of the bigger peripheral catheter that was designed with an enhanced penetration depth to visualize the entire vessel wall, the larger proximal iliac artery (average diameter 6.8 mm based on *in vivo* IVUS measurements) of one animal was imaged with the 9F/15MHz cNIRF-IVUS. In the latter case, intra-arterial access was achieved with a 9F introducer sheath in the right femoral artery. Then, a 20 mm long, 4 mm non-compliant balloon was inflated to 10 atmospheres three times for one minute each, to induce injury. Subsequently, we intravenously injected the FDA-approved NIRF agent, indocyanine green (0.25 mg/kg, i.v.). ICG illuminates atheroma in areas of increased vessel permeability and compromised endothelial barrier integrity[76]. Approximately 90 minutes after ICG injection, intravascular cNIRF-IVUS imaging of the iliac artery was performed using the 9F/15MHz catheter for imaging larger diameter vessels.

After sacrifice, the injured vessel was harvested on ice and multichannel *ex vivo* FM (Kodak ImageStation 4000, Carestream Health) performed for white light (WL), autofluorescence (FITC, excitation/emission 470/535 nm), and ICG (Cy7,

excitation/emission 740/790 nm). The tissue was then freshly frozen in optimal

cutting temperature compound and serial 7 μm cryostat sections obtained.

Tissue cross-sections were evaluated by fluorescence microscopy (Nikon Eclipse

90i) for autofluorescence, and ICG. Co-registration between cNIRF-IVUS,

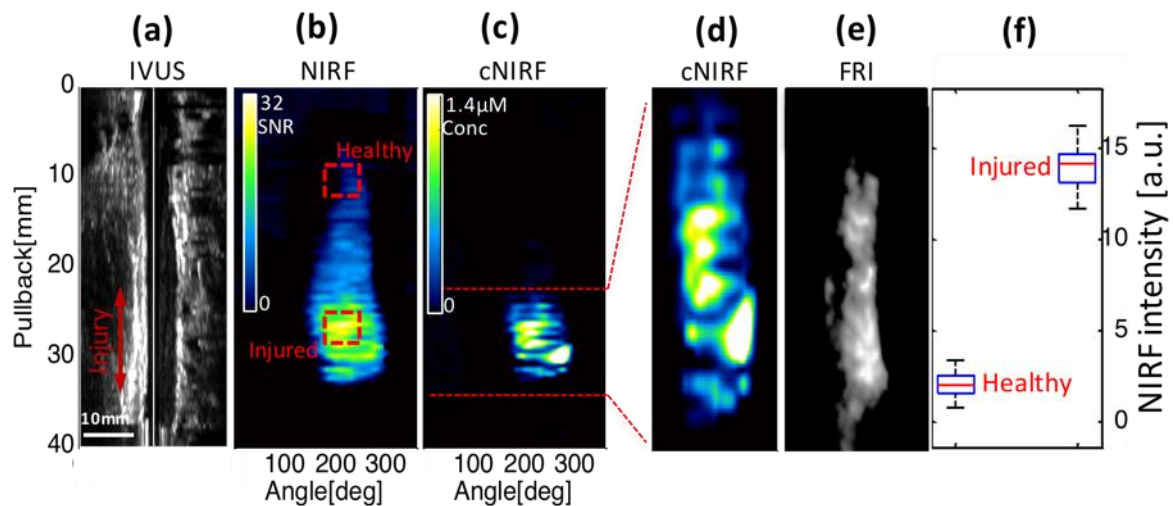standalone IVUS, and histological cross-sections was performed using fluidical

markers.

Figure 30. In vivo cNIRF-IVUS imaging of ICG after arterial injury. (a) Ultrasound longitudinal image of the injured artery, without clear evidence of vascular injury. (b) The corresponding raw NIRF image of the injured artery clearly outlines areas of ICG-demarcated vascular injury induced by the angioplasty balloon. Red doted squares outline areas used to compare signals from healthy and injured regions. (c) NIRF image corrected for blood attenuation reveals that the NIRF ICG signal enhancement is focal. Images in (d) and (e) represent the expanded view of the raw and distance-corrected NIRF signal from the injured area of the artery. (f) NIRF intensities from healthy and injured regions shown in (b).

The cNIRF-IVUS system obtained images of the iliac artery *in vivo* through blood.

Architecture of the vessel visualized by means of IVUS is shown in **Figure 30a**.

ICG NIRF signal localized to the injured artery (**Figure 30b**), indicating altered

pathophysiology that was not evident on standalone IVUS. The distance-

corrected NIRF image of the injured area (**Figure 30c**) revealed that fluorescence signal is more focal. Good visual correlation was observed when compared to fluorescence distribution obtained by FRI (**Figure 30e**). The target-to-background ratio between fluorescence intensities collected from the injured and healthy vessel areas (highlighted with red dashed squares in **Figure 30b**) was calculated to be 24 dB (**Figure 30f**).
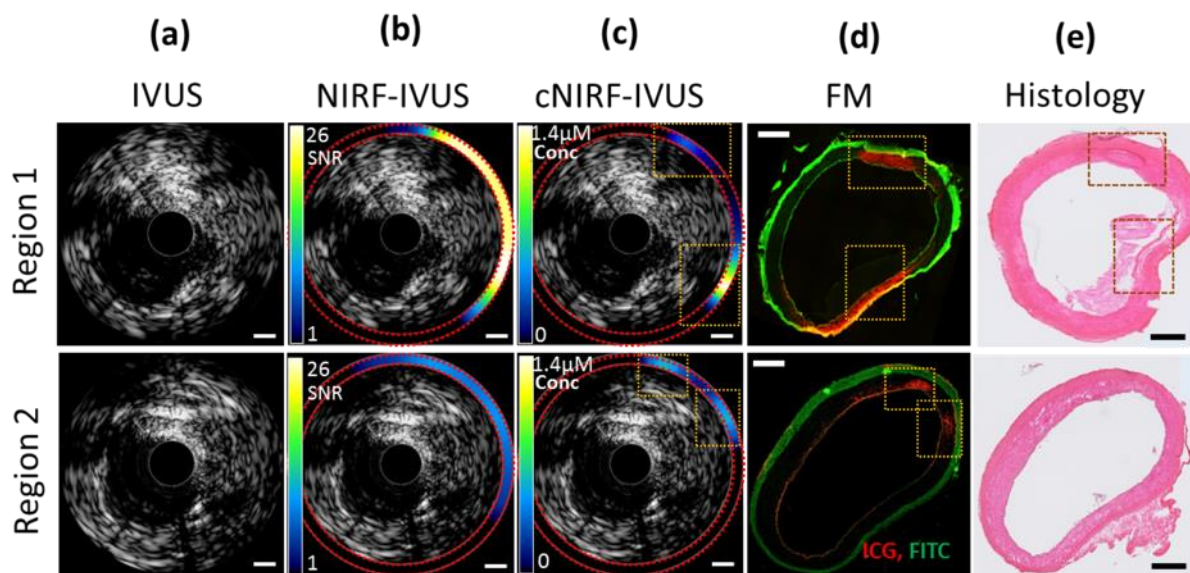

Figure 31. Ex vivo validation of the in vivo cNIRF-IVUS imaging of ICG arterial injury. Comparison of the standalone IVUS (a), and the integrated NIRF-IVUS cross sectional images before (b) and after(c) blood attenuation correction with fluorescence microscopy (FM) slices (d). The standalone anatomical IVUS image does not provide clear evidence of angioplasty-induced injury in the vessel wall. Injury demarcated by ICG deposition is clearly recognized on the cNIRF-IVUS fusion images in both Region 1 and Region 2, as confirmed by fluorescence microscopy (FM images, red dotted boxes). Red pseudocolor in the vessel wall depicts ICG deposition in the NIR channel, and green pseudocolor is arterial wall autofluorescence in the 488 nm channel. FM images acquired, processed and windowed identically. Scale bars in NIRF and cNIRF images, 1 mm. Scale bar in FM images, 0.5 mm. (h) Histology of the corresponding slices. Scale bars 0.5 mm.

Next, the importance of the *in vivo* distance correction algorithm was demonstrated on axial cNIRF-IVUS images. As shown in **Figure 31**, distance

correction improved the agreement between *in vivo* cNIRF signals (**Figure 31c**) and ICG NIRF fluorescence obtained *ex vivo* with fluorescence microscopy (**Figure 31d**, red). Correlation increased from 36% to 58% in Region 1 and from 61% to 69% in Region 2. Compared to standalone IVUS images, 2D cNIRF images readily and comprehensively identified areas of angioplasty-induced vascular injury. Finally, histological analysis further validated our findings as shown in **Figure 31e**.

To further validate ability of the 4.5F/40MHZ cNIRF-IVUS catheter to detect ICG in vascular injury model was further assessed with additional *in vivo* imaging studies performed in the femoral artery of another swine (N=2) using the 4.5F/40MHz cNIRF-IVUS catheter and detailed histological correlation. Therefore, after obtaining antegrade intra-arterial access with a 6 French introducer sheath in the common iliac artery, vascular injury was performed in the distal femoral artery using a 4.0x20mm angioplasty balloon inflated to 10 atm for 1 min three times. Subsequently, ICG (0.25 mg/kg) was administered intravenously, followed by Evans blue (EB; 50 ml of 5% solution) 30 min later, to assess impaired endothelial permeability. Ninety minutes after ICG injection, 40 mm cNIRF-IVUS pullbacks were performed across the injured zone.

Ex vivo imaging procedures were identical to ones described before. Additionally, histological cross-sections were stained for elastin with Verhoeff-

Van Gieson (VVG; Elastic Stain Kit HT254; Sigma-Aldrich) to identify disruptions of the elastic lamina, followed by immunohistochemistry to detect endothelial damage (CD31 clone LCI-4, 1:100 dilution; Santa Cruz Biotechnology). Using a MACH2 labeled AP polymer secondary visualized with Vulcan fast red chromagen (Biocare Medical).

Figure **Figure 32a** demonstrates longitudinal view IVUS image which revealed topography of the femoral artery after balloon injury. The corresponding cNIRF image map shows elevated *in vivo* NIRF ICG signal focally at the location where balloon injury was performed, with negligible NIRF signal (blue/black pseudocolor) in the flanking non-injured regions (**Figure 32b**). **Figure 32c** and **d** represent the multichannel fluorescence microscopy of a tissue cross-section from the location corresponding to the cNIRF-IVUS image shown in **Figure 32a** and **b**. The region of the white dotted box in **Figure 32c** is presented in a magnified view in **Figure 32d**. ICG uptake (red pseudocolor) associated with Evans Blue (EB, green pseudocolor) signal distinct from autofluorescence (AF, blue pseudocolor) tissue background signal, indicating that the mechanism of ICG entry into the arterial wall was related to an impaired endothelial barrier. A control, non-injured femoral artery demonstrated no ICG signal uptake by fluorescence microscopy (**Figure 32g**), that was associated with an intact endothelial layer by CD31 immunohistochemistry (**Figure 32e**).
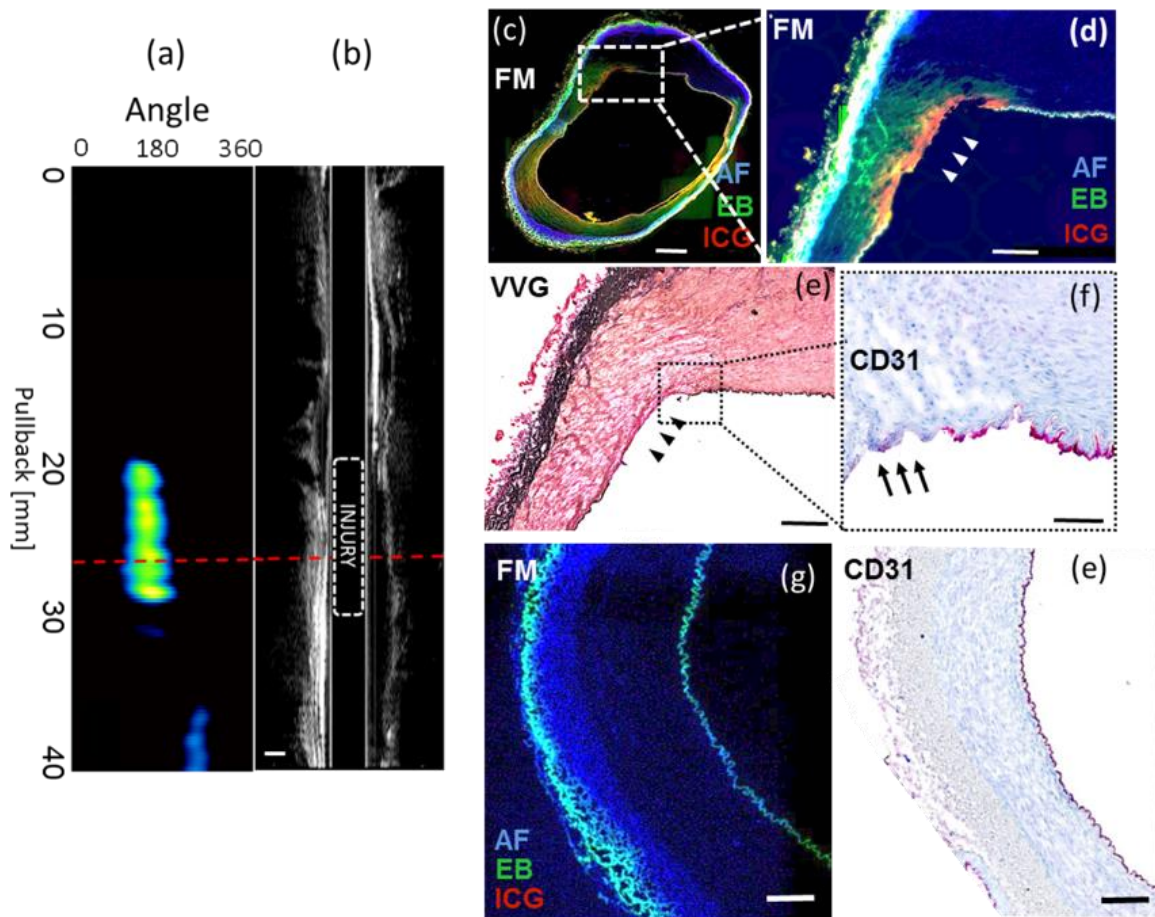
Figure 32. cNIRF-IVUS imaging of angioplasty-induced vascular injury. (a) The cNIRF image map demonstrates ICG uptake in the area of angioplasty against negligible NIRF background signal (blue/black pseudocolor. (b) Longitudinal view IVUS image. (c) Sections stained for elastin showed that ICG deposited in the arterial media around injury, ICG -red pseudocolor, Evans Blue (EB) - green pseudocolor, autofluorescence (AF) - blue pseudocolor. Scalebar 500 μm. (d) Magnified view of the region highlighted with white doted box in (c). Scalebar 250 μm. (e) Histological staining of adjacent matching section. VVG - Verhoeff Van Gieson. Black arrowheads indicate injured zone. Scale bar 250 μm. (f) Disruption of the internal elastic lamina shown by CD31 immunohistochemistry. Pink = positive CD31 immunostaining. Black arrowheads indicate injured zone. Scale bar 100 μm. (g) FM of a control, non-injured femoral artery. No ICG signal uptake was observed. (e) An intact endothelial layer by CD31 immunohistochemistry. Scale bars in (g) and (e) are 200 μm.

Thus, we demonstrated ability of both 9F/15MHz and 4.5F/45MHz catheters to detect ICG *in vivo*. We further found that leaking of ICG into the media is localized with disruption of endothelial barrier – one of the important pathobiological parameters associated with atherosclerosis and restenosis. Detection of *in vivo*

vascular alterations by cNIRF-IVUS beyond standalone IVUS offers a novel and powerful imaging approach for research of vascular injuries, and extends the applications of ICG and related targeted NIRF imaging probes beyond atherosclerosis detection[76].

6.3 cNIRF-IVUS Detection of Prosense VM110

To demonstrate cNIRF-IVUS imaging of a fluorescence dye Prosence VM110, we employed a modified New Zealand White rabbit atherosclerosis model (MGH IACUC **Protocol #2013N000015**) that generates highly-inflamed, aortic plaques[90]. Following two weeks of high-cholesterol diet (4.7% coconut oil-based, 1% total cholesterol; Research Diets Inc.), the rabbit underwent aortic balloon-injury (3F Fogarty; Edwards Lifesciences) and continued 1% high-cholesterol diet for 4 weeks followed by 4 weeks of normal cholesterol chow. At 8 weeks post-injury, the rabbit was imaged with 4.5F/40MHz cNIRF-IVUS catheter 24 hours after intravenous injection of a protease-activatable imaging reporter (Prosense VM110, 4 mg/kg IV; PerkinElmer). The day of imaging, the rabbit was anestheterized with ketamine (35 mg/kg) and xylazine (3.5 mg/kg), a 5F sheath was placed in the carotid artery and heparin (IV 100 U/kg) was administered. A 70mm cNIRF-IVUS pullback through blood was performed with rotation speed of 120 rpm.

Distance-corrected cNIRF image clearly revealed two areas (12-30mm and 38-50

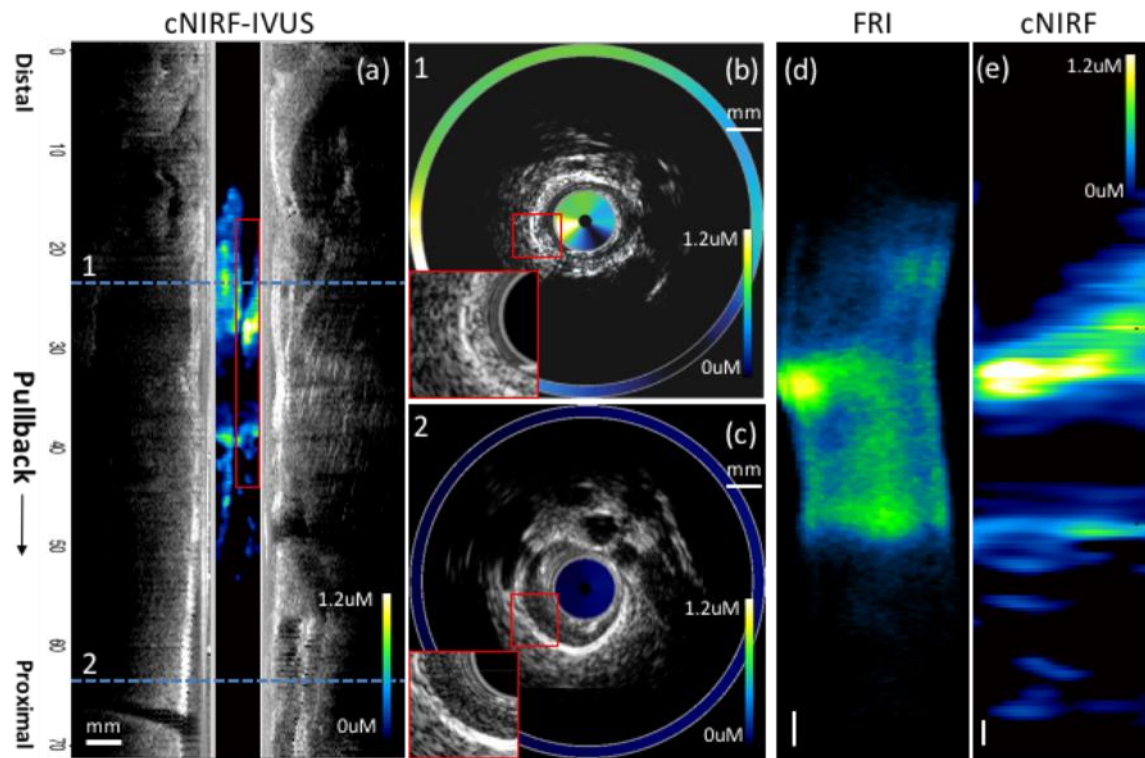mm   at

Figure 33 and **e**) of elevated NIR signal with a 7mm lower NIRF signal region in

between. The same fluorescence distribution was observed on the *ex vivo* FRI

image of the resected artery (**Figure 33d**). Representative cross-sectional cNIRF-
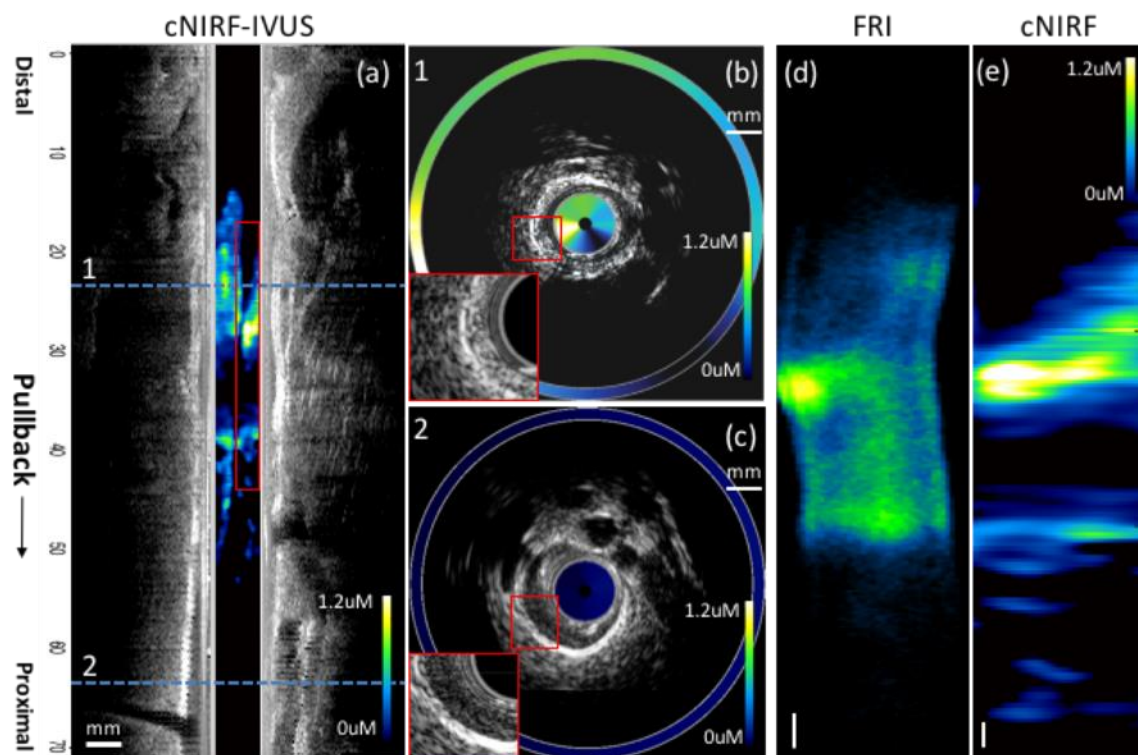
IVUS images are shown in **Figure 33b** and **c**.

Figure 33. In vivo cNIRF-IVUS imaging of atherosclerosis. Fused longitudinal ultrasound (black and white) and cNIRF images of the rabbit atheroma. Representative cNIRF-IVUS cross-sectional images in the pullback position 1 and 2 are shown in (b) and (c), with lower left magnified insets demonstrating evidence of atherosclerosis at position 1 in (b). The ex vivo fluorescence reflectance image (FRI) of the resected artery (d) correlated with the cNIRF image (e). Scale bars, 1 mm for all images.

Here, we showed, that cNIRF-IVUS can detect Prosense VM110 *in vivo*. This result is of particular importance since cysteine protease such as cathepsin B, S and L could be used as effective imaging targets for plaque inflammation as they are being significantly upregulated at the sites of plaque rupture[70,91,92] and can be detected by means of Prosense VM110[70,93], providing further molecular information additional to ICG.

6.4 cNIRF-IVUS Imaging in Presence of a Metal Coronary Stent

In the next experiment, we investigate cNIRF-IVUS imaging in presence of metal stent. Therefore, a 2.75 by 12 mm coronary bare metal stent bearing human fibrin labeled with a fibrin-targeted NIRF peptide molecular imaging agent was implanted into the right coronary artery of a swine, followed by 40 MHz cNIRF-IVUS imaging *in vivo*. To prepare the NIRF stent, we first incubated a coronary stent (Multi-Link Vision 2.75x12mm, Abbott Vascular) coated with fluorescent fibrin clots via a fibrin-targeted peptide conjugated to an NIR fluorochrome[94]. Human clots were created from fresh frozen plasma (FFP) obtained via a protocol approved by the Partners Internal Review Board (#2004P001401). First, a centrifuge tube was filled with 180 µL of FFP. The stent was next immersed into the FFP and then 10 µL of 0.4 M CaCl2, 10 µL of thrombin, and 12 µL of FTP11-Cy7 was added to induce clot formation around the stent[28]. This mixture was incubated at 37 °C for approximately 24 hours. Stent was implanted based on a standard protocol for angioplasty. Sequentially, 4.5F/40MHz cNIRF-IVUS catheter was introduced through a 6F introducer and 30 mm long imaging pullback was at rotational speed 80 rpm and a 0.2 mm pullback step. Such a rotation speed was chosen in order to match the intrinsic heart rate and thus potentially reduce motion artifacts[95,96].

As **Figure 34a** exhibits, IVUS revealed the architecture of the coronary artery. Although the rotational speed was matched approximately to the heart rate, ultrasound B-scan images still suffered from motion artifacts, similar to standalone clinical IVUS coronary images[97–99]. Simultaneously acquired co-registered NIRF data allowed molecular imaging of the fibrin content within the stent (**Figure 34b**). Despite metal sent struts which could block fluorescence signals, when compared to *ex vivo* FRI (**Figure 34c**), a strong visual correlation of the detected fluorescence distribution was observed within the stented region. The harvested vessel was cut open, and its inner surface containing the stent underwent epifluorescence microscopy (**Figure 34f**). To appreciate effect of distance correction, correlation of FM image with NIRF (**Figure 34d**) and cNIRF (**Figure 34e**) images was computed. Correlation coefficient increased from R=0.68 to R=0.74 after correction. Also, some features of the fluorescence image not initially visible on the raw NIRF image (**Figure 34d**, areas 1 and 2) were recovered after distance correction (**Figure 34e**, areas 1 and 2).
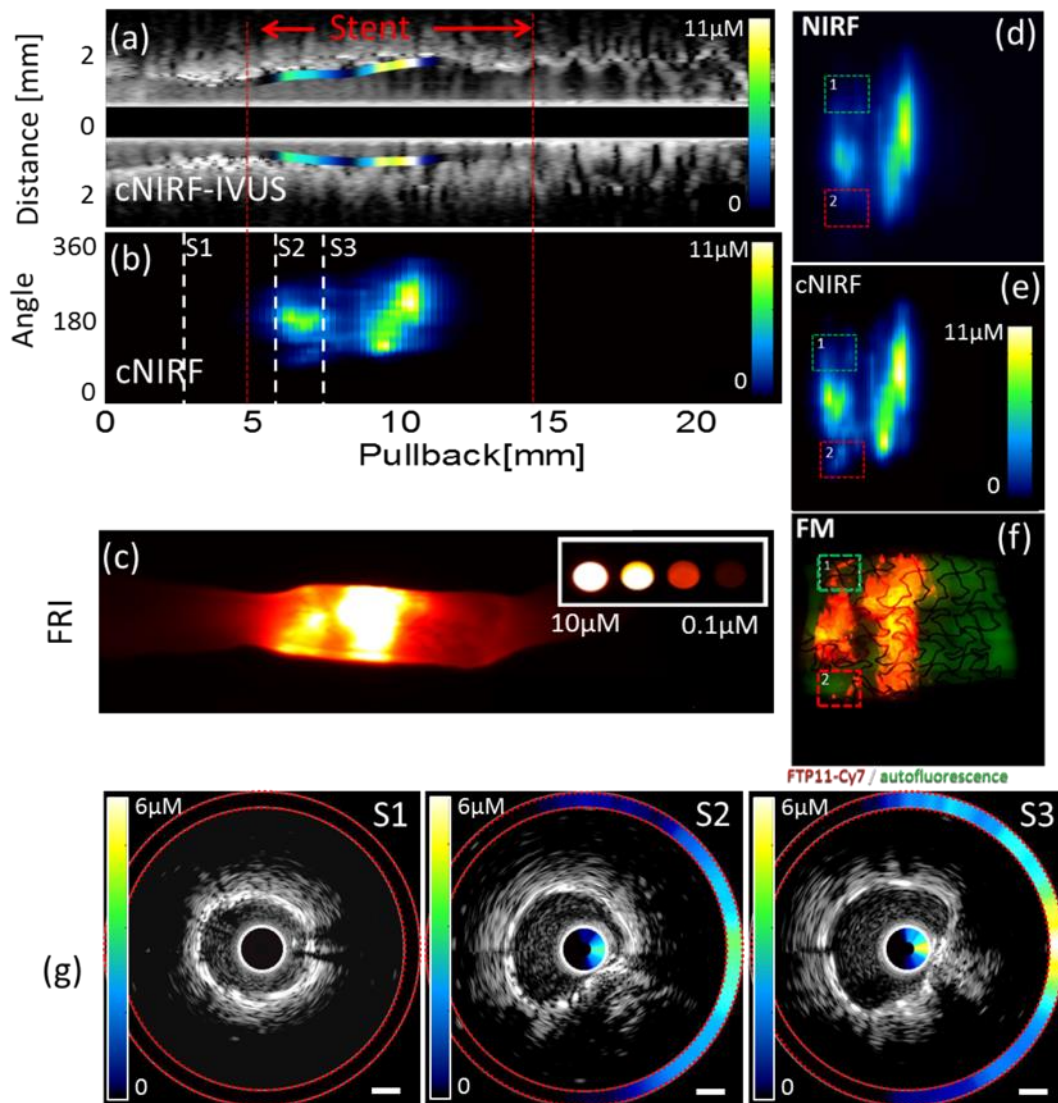
Figure 34. In vivo imaging of the coronary artery with an implanted NIR fluorescent fibrin-labeled stent. (a) Longitudinal cNIRF-IVUS image of the artery obtained with 40 MHz hybrid catheter. (b) Distance-corrected cNIRF signal measured in vivo through blood. (c) Fluorescence reflectance image (FRI) of the artery. (e) Expanded view of the uncorrected NIRF image. Expanded view of the distance-corrected cNIRF image (e) shows good visual correlation with distribution of NIR fluorescence activity co-registered on inner surface of the vessel ex vivo by fluorescence microscopy (FM) shown in (f). Pseudocolor: FTP11-Cy7, orange; autofluorescence; green. Area 1 and 2 were not visible on the raw NIRF image (d), but were recovered as result of distance correction. (g) Representative examples of the cross-sectional cNIRF-IVUS images corresponding to pull back positions S1, S2 and S3 in (a) and (b). The cNIRF signal is fused on to the interior and exterior of the IVUS catheter. Scale bar, 1 mm.

Herein we showed, that cNIRF-IVUS can visualize fluorescence distribution also

inside a metal stent. No significant NIRF artifacts were noticed due to stent

struts. Concurrent morphological and molecular imaging was demonstrated useful for detection of fibrin deposits on a coronary stent.

6.5 cNIRF-IVUS Imaging of a Healthy Vessel

To confirm cNIRF-IVUS imaging, a healthy vessel was imaged as a control. The imaging protocol was identical to one described in Chapter 6.4, but without injection of fluorescent dye. Shortly, male Yorkshire pig was anesthetized using telazol (4.4 mg/kg) and xylazine (2.2 mg/kg), followed by isoflurane (Patterson Veterinary Supply, Devens, MA, USA). Intra-arterial access was achieved using 6 French sheath placed into the distal carotid artery. Then, 4.5F/40MHz cNIRF-IVUS catheter was forwarded to the LAD artery and a 30mm pullback was performed.

Figure 35a and **Figure 35b** show cNIRF-IVUS image of the LAD artery. Amplitude of the detected cNIRF signals were measured to be below 0.05 µM, what is ~10 times smaller compared to signals shown in **Figure 34**. Also, there was no distinctive fluorescence pattern detected. Representative cNIRF-IVUS cross section images are shown in **Figure 35c** and **Figure 35d**. This result confirms that NIRF signals detected with the engineered cNIRF-IVUS system are attributed to accumulation of fluorescence dyes.
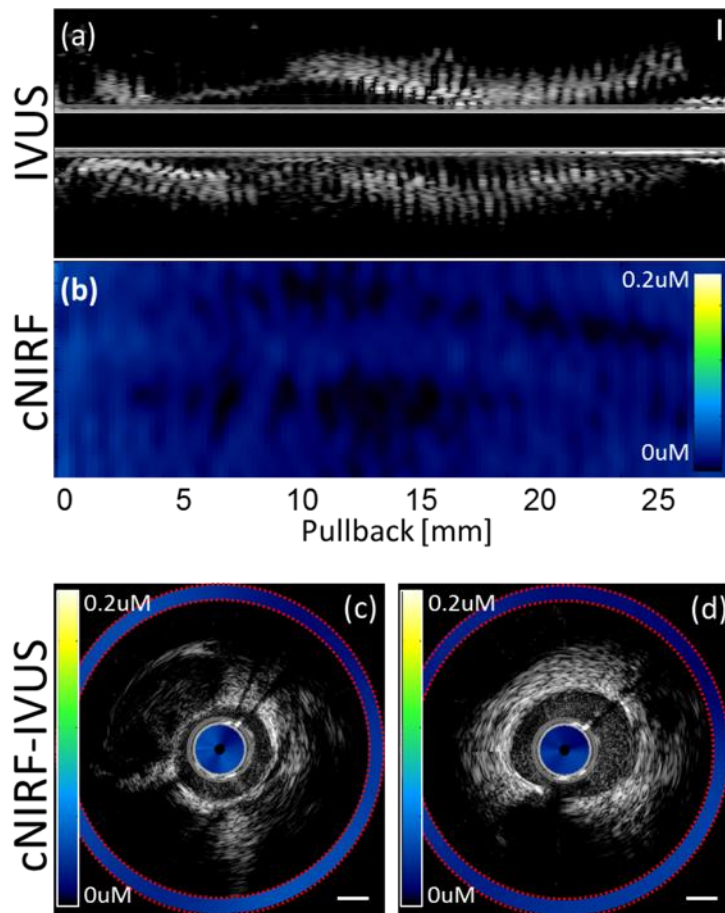
Figure 35. cNIRF-IVUS images of the healthy control vessel. IVUS image (a) of the LAD artery was acquired simultaneously with cNIRF image (b) in vivo. Representative cNIRF-IVUS cross sections are shown in (c) and (d). All scale bars are 1mm.

6.6 Discussion

IVUS is the prevailing intravascular clinical imaging modality worldwide, but currently it assesses only morphological disease features and it lacks the contrast to image biological or pathophysiological markers involved in arterial disease. Since *in vivo* assessment of disease biology is important for better understanding of disease progression and for therapy evaluation, new approaches are needed to visualize the *in vivo* biology of atheroma and endovascular injury at early stages of progression and after angioplasty or stenting. The novel intravascular

cNIRF-IVUS technique superimposes accurate fluorescence molecular imaging readings through blood onto conventional IVUS anatomical views, possibly enabling a paradigm shift beyond stand-alone IVUS.

During our investigations, we observed that raw fluorescence intensities collected by the NIRF system on its own depend on the distance between the vessel wall and the catheter, due to distance-related attenuation by blood, which can lead to unreliable results and inaccurate observations when imaging *in vivo*. A particular novelty of the work herein is the development and *in vivo* confirmation of a blood-related attenuation correction scheme that is shown to improve the imaging accuracy of the hybrid system over stand-alone NIRF implementations in blood-filled arteries. This correction scheme enables quantitative fluorescent readouts for the first time. In contrast to previously reported systems[29,30] where the ultrasound transducer rotated independently from the NIRF detector, it is the first cNIRF-IVUS system where reliable co-registration of the morphology and fluorescence intensities is achieved by engineering an all-in-one rotating detector. Importantly, unlike previous cNIRF-IVUS studies[29,30,66], where blood attenuation parameters were assigned based on *ex vivo* observations or historical empirical measurements, the present analysis utilized *in vivo* session-specific estimation of blood attenuation.

The importance of the fluorescence dimension, over other hybrid possibilities such as optoacoustic imaging[100] or spectral imaging[21], is that the use of fluorescence agents enables contrast engineering to illuminate molecular details of interest. In other words, NIRF imaging is not limited to visualizing one or a few parameters (e.g. lipid content); rather, depending on the agent employed, it can potentially sense a very large number of disease biomarkers, such as markers of increased permeability and inflammation[76], protease activity[26], apoptosis and other parameters associated with vascular disease[6]. Initially considered a remote possibility, targeted fluorescence agents are now gaining approval for clinical use in the context of clinical trials in cancer surgical or endoscopic guidance[24]. Therefore, there is imminent potential to translate this cancer-related example to CAD theranostic and possibly diagnostic applications.

The concept of a fluorescence-based hybrid system has also been demonstrated using simultaneous NIRF and OCT imaging[28,81]. In contrast to IVUS, OCT is involved in a fraction of intravascular imaging procedures performed worldwide. Nonetheless, the development of hybrid NIRF-OCT further underscores the importance of the fluorescence dimension in adding biology reading to a morphology imaging modality. Unlike cNIRF-IVUS, NIRF-OCT is limited to imaging of superficial layers of the vascular wall and cannot be performed through blood, since OCT requires flushing and displacement of blood. Conversely, near-infrared

fluorescence detection can visualize structures up to cm deep and integrate molecular imaging onto IVUS readings without the need for blood occlusion or flushing, allowing operation with standard clinical workflow protocols with IVUS.

The cNIRF-IVUS demonstration was performed herein with two different catheters, a 4.5F/40MHz implementation for investigating smaller lumens (coronary arteries) and a 9F/15MHz design employed to image larger arteries. Using an ultrasound transducer with higher central frequency helped to resolve finer morphological details with lateral resolution of 300 µm and axial resolution of 150 µm, while using a lower-frequency transducer enabled imaging of structures up to 20 mm deep inside the vessel wall. We found that the detection sensitivity of the NIRF modality allowed imaging through ~2 mm of blood when AlexaFluor750 or ICG was used as a fluorescence dye. A catheter system with a sheath with a diameter of 2 mm should allow imaging of vessels 6 mm wide. Larger vessels can be imaged by further improving the NIRF detection sensitivity and/or quantum yield of fluorescence dyes. If the ultrasound transducer is engineered to sit in series with the fiber tip, instead of parallel with the tip as in the present work, it may be possible to reduce the total diameter of the cNIRF-IVUS catheter to 1 mm (3 French) or less, which would further facilitate intracoronary imaging of small vessels.

Here cNIRF-IVUS was shown to visualize fibrin deposition on coronary stent struts *in vivo*. As fibrin deposition is pathophysiologically implicated in stent thrombosis[101,102], this result demonstrates the potential of the cNIRF-IVUS system to detect unhealed stents at risk of stent thrombosis, a complication that routinely leads to myocardial infarction or death[103].

The cNIRF-IVUS system can detect ICG accumulation *in vivo* as a result of angioplasty-induced vascular injury far more easily than stand-alone IVUS. The observed NIRF detection of arterial injury extends the applications of ICG beyond that of targeting atherosclerosis reported in Vinegoni et al.[76] We also found that areas of ICG-based fluorescence signals are associated with damage in the endothelial layer. Loss of endothelial integrity allows penetration of ICG molecules into the vessel wall matrix, giving rise to fluorescence signal. Endothelial damage may indicate coronary dissections or arterial injury after stenting, which are associated with poorer outcomes[104]. ICG-enhanced cNIRF-IVUS imaging might offer a new approach to sensitively diagnose coronary pathologies at an early stage and help optimize percutaneous coronary intervention.

Imaging through blood of NIRF signals associated with inflammation in atherosclerosis was also demonstrated with the hybrid approach and mapped with IVUS images captured at the same time. In contrast to prior work with

stand-alone NIRF imaging[26], the cNIRF-IVUS system provides distance correction that allows detection of plaque inflammation in a quantitative manner.

Overall, the results described here demonstrate that concurrent intravascular cNIRF and IVUS offer molecular and morphological detection of arterial wall pathology through flowing blood in coronary and larger arteries *in vivo*. The performance of cNIRF-IVUS, as assessed *ex vivo* and *in vivo*, demonstrated improvements in imaging fidelity and accuracy compared to raw NIRF images, as confirmed by FRI, histological analysis and fluorescence microscopy. Attenuation correction is necessary to reduce errors caused by variable signal attenuation in blood, and it can significantly improve the reliability of NIRF measurements.

7 Conclusions

The **first** major contribution of this work is the engineering, characterization, and validation of the hybrid cNIRF-IVUS catheter system for co-registered molecular and morphological imaging. An NIRF detector with improved sensitivity and an ultrasound transducer were integrated into an intravascular endoscope to enable reliable imaging through flowing blood. A 9F/15MHz hybrid cNIRF-IVUS catheter was specifically designed for experiments in larger arteries (carotid, iliac), and a 4.5F/40MHz catheter was designed for experiments in coronary arteries. We investigated (a) sensitivity and resolutions of both NIRF and IVUS modalities; (b) reproducibility of cNIRF-IVUS imaging through blood *in vivo*; (c) capacity of the cNIRF-IVUS imaging system to provide quantitative NIRF data; (d) ability to image large (>5 mm) and small (<5 mm) vessels, also in presence of metallic stents; (e) ability to visualize *in vivo* accumulation of fluorescent agents including ICG and Prosense VM110. All *in vivo* findings were confirmed by fluorescence microscopy, fluorescence reflectance imaging and/or histology analysis.

The **second** major contribution of this work is the development of a novel NIRF correction algorithm. We showed that the developed method can adaptively operate on each fluorescent measurement obtained and correct it for catheter-vessel-wall distance and blood attenuation based on IVUS images to retrieve the

true fluorescence intensity on the surface of the vessel wall. The algorithm is applicable only to the hybrid system, whereby concurrent measurements of fluorescence intensity (by NIRF) and of distance (by IVUS) are introduced into a global minimization problem, which is solved for blood attenuation. We demonstrated clear improvement in imaging accuracy, compared to uncorrected images, as confirmed by multiple *ex vivo* imaging modalities.

The **third** important finding was a significant difference in blood attenuation of detected fluorescence signals between *in vivo* and *ex vivo* settings. This discovery means that distance-correction algorithms obtained empirically from *ex vivo* data, may not be appropriate for correcting *in vivo* results. *Ex vivo* correction schemes overestimate the degree of light attenuation that occurs *in vivo*. In contrast to previous works, we based our distance correction exclusively on *in vivo* calibration measurements.

The **fourth** major contribution of this thesis work is validation of cNIRF-IVUS imaging in clinically relevant *in vivo* scenarios such as (a) detection of iliac arterial injury following angioplasty, (b) imaging of fibrin deposition on a coronary stent, and (c) assessment of developed atheroma.

The overall results demonstrate that IVUS, the dominant intravascular imaging modality worldwide, can be extended with the NIRF modality to provide

molecular-structural imaging in protocols identical to clinical IVUS imaging through blood.

Future efforts are ongoing to develop a clinical-grade intravascular cNIRF-IVUS catheter for human coronary arterial molecular-structural imaging. This clinical system will offer frame rates of 30/sec with a 4F-compatible clinical catheter. In parallel, a triple-mode catheter will be developed for cNIRF, IVUS, and optoacoustic (OA) imaging. Subsequently, the triple modality cNIRF-IVUS-OA will be expanded with multispectral optoacoustics (MSOA), which does not require catheter re-engineering. This will empower the system by allowing it to exploit additional endogenous contrast. For example, MSOA can detect fat by its absorption peak around 930 nm, allowing MSOA to image lipid-rich atherosclerotic plaques[105]. With a tri-modal catheter, it may be possible to characterize plaques in order to assess their risk of rupture, which can lead to acute coronary events[85]. We hypothesize that MSOA imaging will also enable calibration of the correction algorithm on a per-rotation basis to adapt normalization parameters for varying optical properties of blood and, thereby, further improve the quantitative ability of the system.

8 References.

1. Townsend, N., Nichols, M., Scarborough, P. & Rayner, M. Cardiovascular disease in Europe - Epidemiological update 2015. *Eur. Heart J.* **36,** 2696–2705 (2015).

2. Naghavi, M. *et al.* From Vulnerable Plaque to Vulnerable Patient: A Call for New Definitions and Risk Assessment Strategies: Part II. *Circulation* **108,** 1772–1778 (2003).

3. Naghavi, M. *et al.* Review : Current Perspective From Vulnerable Plaque to Vulnerable Patient A Call for New Definitions and Risk Assessment Strategies : Part I Vulnerable Patient : Part I. *Circulation* **108,** 1664–72 (2003).

4. Chen, I. Y. & Wu, J. C. Cardiovascular molecular imaging: Focus on clinical translation. *Circulation* **123,** 425–443 (2011).

5. Naghavi, M. *et al.* From Vulnerable Plaque to Vulnerable Patient: A Call for New Definitions and Risk Assessment Strategies: Part II. *Circulation* **108,** 1772–1778 (2003).

6. Sanz, J. & Fayad, Z. A. Imaging of atherosclerotic cardiovascular disease. *Nature* **451,** 953–957 (2008).

7. Wikipedia-Atherosclerosis. (2006). at <https://en.wikipedia.org/wiki/Atherosclerosis>

8. Diethrich, E. B. *et al.* Intravascular ultrasound imaging of iliac stenoses during endovascular surgery. *J. Cardiovasc. Technol.* **8,** 287–293 (1989).

9. Garcia-Garcia, H. M., Costa, M. A. & Serruys, P. W. Imaging of coronary atherosclerosis: Intravascular ultrasound. *Eur. Heart J.* **31,** 2456–69 (2010).

10. Tearney, G. J. *et al.* Three-Dimensional Coronary Artery Microscopy by Intracoronary Optical Frequency Domain Imaging. *JACC Cardiovasc. Imaging* **1,** 752–761 (2008).

11. Yabushita, H. *et al.* Characterization of human atherosclerosis by optical coherence tomography. *Circulation* **106,** 1640–1645 (2002).

12. Prati, F. *et al.* Expert review document on methodology, terminology, and clinical applications of optical coherence tomography: Physical principles, methodology of image acquisition, and clinical application for assessment of coronary arteries and atherosclerosis. *Eur. Heart J.* **31,** 401–415 (2010).

13. Li, X. *et al.* High-resolution co-registered intravascular imaging with integrated high frequency ultrasound and OCT probe. *Proc. - IEEE Ultrason. Symp.* **97,** 1506–1509 (2010).

14. Yin, J. *et al.* Integrated intravascular optical coherence tomography ultrasound imaging system. *J. Biomed. Opt.* **15,** 10512 (2010).

15. Suter, M. J. *et al.* Intravascular optical imaging technology for investigating the coronary artery. *JACC Cardiovasc. Imaging* **4,** 1022–1039 (2011).

16. Manfrini, O. *et al.* Sources of error and interpretation of plaque morphology by optical coherence tomography. *Am J Cardiol* **98,** 156–159 (2006).

17. Pu, J. *et al.* Insights into echo-attenuated plaques, echolucent plaques, and plaques with spotty calcification: Novel findings from comparisons among intravascular ultrasound, near-infrared spectroscopy, and pathological histology in 2,294 human coronary artery segment. *J. Am. Coll. Cardiol.* **63,** 2220–2233 (2014).

18. Rudd, J. H. F. *et al.* Imaging Atherosclerotic Plaque Inflammation With [18F]-Fluorodeoxyglucose Positron Emission Tomography. *Circulation* **105,** 2708–2711 (2002).

19. Hyafil, F. *et al.* Noninvasive detection of macrophages using a nanoparticulate contrast agent for computed tomography. *Nat. Med.* **13,** 636–41 (2007).

20. Ruehm, S. G., Corot, C., Vogt, P., Kolb, S. & Debatin, J. F. Magnetic Resonance Imaging of Atherosclerotic Plaque With Ultrasmall Superparamagnetic Particles of Iron Oxide in Hyperlipidemic Rabbits. *Circulation* **103,** 415–423 (2016).

21. Brugaletta, S. *et al.* NIRS and IVUS for characterization of atherosclerosis in patients undergoing coronary angiography. *JACC Cardiovasc. Imaging* **4,** 647–655 (2011).

22. Zhang, J., Yang, S., Ji, X., Zhou, Q. & Xing, D. Characterization of lipid-rich aortic plaques by intravascular photoacoustic tomography: Ex vivo and in vivo validation in a rabbit atherosclerosis model with histologic correlation. *J. Am. Coll. Cardiol.* **64,** 385–390 (2014).

23. Fatakdawala, H. *et al.* Fluorescence Lifetime Imaging Combined with Conventional Intravascular Ultrasound for Enhanced Assessment of Atherosclerotic Plaques: an Ex Vivo Study in Human Coronary Arteries. *J. Cardiovasc. Transl. Res.* **8,** 253–263 (2015).

24. van Dam, G. M. *et al.* Intraoperative tumor-specific fluorescence imaging in ovarian cancer by folate receptor-α targeting: first in-human results. *Nat. Med.* **17,** 1315–9 (2011).

25. Atreya, R. *et al.* In vivo imaging using fluorescent antibodies to tumor necrosis factor predicts therapeutic response in Crohn's disease. *Nat. Med.*

20, 313–8 (2014).

26.   Jaffer, F. A. *et al.* Two-dimensional intravascular near-infrared fluorescence molecular imaging of inflammation in atherosclerosis and stent-induced vascular injury. *J. Am. Coll. Cardiol.* **57,** 2516–2526 (2011).

27.   Jaffer, F. A., Libby, P. & Weissleder, R. Optical and multimodality molecular imaging: Insights into atherosclerosis. *Arterioscler. Thromb. Vasc. Biol.* **29,** 1017–1024 (2009).

28.   Yoo, H. *et al.* Intra-arterial catheter for simultaneous microstructural and molecular imaging in vivo. *Nat. Med.* **17,** 1680–4 (2011).

29.   Dixon, A. J. & Hossack, J. A. Intravascular near-infrared fluorescence catheter with ultrasound guidance and blood attenuation correction. *J. Biomed. Opt.* **19,** 20901 (2014).

30.   Mallas, G. *et al.* Improving quantification of intravascular fluorescence imaging using structural information. *Phys. Med. Biol.* **57,** 6395–6406 (2012).

31.   WangV., L. hsin-I. *Biomedical Optic Principles and Imaging*. (John Wiley & Sons, 1391). at <https://books.google.com/books?id=EJeQ0hAB76gC&pg=PA175&lpg=PA175&dq=biomedical+optic+principles+and+imaging++++lihung+v.wang+and+hins&source=bl&ots=k7ierTsSGZ&sig=3nyATQWh5e1NC2dhKK76qYLalNY&hl=en&sa=X&ved=0ahUKEwjIzfPLgozKAhUqJnIKHSLTDE0Q6AEIMjAD#v=onep>

32.   Zhun310. Near-infrared window in biological tissue. (2009). at <https://en.wikipedia.org/wiki/Near-infrared_window_in_biological_tissue#/media/File:Fig_1_-_The_molar_extinction_coefficient_of_HbO2_and_Hb.png>

33.   Twersky, V. Absorption and multiple scattering by biological suspensions. *J. Opt. Soc. Am.* **60,** 1084–1093 (1970).

34.   Steinke, J. M. & Shepherd, A. P. Role of Light Scattering in Whole Blood Oximetry. *Ieee Trans. Biomed. Eng.* 294–301 (1986). doi:10.1109/TBME.1986.325713

35.   Steinke, J. M. & Shepherd, A. P. Role of Light Scattering in Spectrophotometric Measurements of Arteriovenous Oxygen Difference. *IEEE Trans. Biomed. Eng.* **BME-33,** 729–734 (1986).

36.   Lipowsky, H. H., Usami, S., Chien, S. & Pittman, R. N. Hematocrit determination in small bore tubes by differential spectrophotometry. *Microvasc. Res.* **24,** 42–55 (1982).

37.   Bosschaart, N., Edelman, G. J., Aalders, M. G. C. G., Van Leeuwen, T. G. & Faber, D. J. A literature review and novel theoretical approach on the

optical properties of whole blood. *Lasers Med. Sci.* **29,** 453–479 (2014).

38. Hu, S., Maslov, K., Tsytsarev, V. & Wang, L. V. Functional transcranial brain imaging by optical-resolution photoacoustic microscopy. *J. Biomed. Opt.* **14,** 40503 (2009).

39. Yaroslavsky, A. N., Yaroslavsky, I. V., Goldbach, T. & Schwarzmaier, H.-J. Optical properties of blood in the near-infrared spectral range. in *Photonics West '96* 314–324 (1996). doi:10.1117/12.239516

40. Roggan, A. *et al.* Optical Properties of Circulating Human Blood in the Wavelength Range 400–2500 nm. *J. Biomed. Opt.* **4,** 36 (1999).

41. Friebel, M. *et al.* Determination of optical properties of human blood in the spectral range 250 to 1100 nm using Monte Carlo simulations with hematocrit-dependent effective scattering phase functions. *J. Biomed. Opt.* **11,** 34021 (2006).

42. Friebel, M. & Helfmann, J. Influence of oxygen saturation on the optical scattering properties of human red blood cells in the spectral range 250to2000nm. *... Opt.* **14,** 34001 (2009).

43. Meinke, M., Müller, G., Helfmann, J. & Friebel, M. Empirical model functions to calculate hematocrit-dependent optical properties of human blood. *Appl. Opt.* **46,** 1742–1753 (2007).

44. Enejder, A. M. K., Swartling, J., Aruna, P. & Andersson-Engels, S. Influence of cell shape and aggregate formation on the optical properties of flowing whole blood. *Appl Opt* **42,** 1384–1394 (2003).

45. Steenbergen, W., Kolkman, R. & de Mul, F. Light-scattering properties of undiluted human blood subjected to simple shear. *J. Opt. Soc. Am. A. Opt. Image Sci. Vis.* **16,** 2959–67 (1999).

46. Friebel, M., Müller, G., Meinke, M. & Helfmann, J. Influence of shear rate on the optical properties of human blood in the spectral range 250 to 1100nm. *J. Biomed. Opt.* **12,** 54005 (2007).

47. Sakota, D. & Takatani, S. Quantitative analysis of optical properties of flowing blood using a photon-cell interactive Monte Carlo code: effects of red blood cells' orientation on light scattering. *J. Biomed. Opt.* **17,** 57007 (2012).

48. Boron, W. F. & Boulpaep, E. L. *Medical Physiology, 2e Updated Edition: with STUDENT CONSULT Online Access*. (Elsevier Health Sciences, 2012). at <https://books.google.com/books?id=54mxMgO5H_YC&pgis=1>

49. Duysens, L. N. M. The flattening of the absorption spectrum of suspensions, as compared to that of solutions. *Biochim. Biophys. Acta* **19,** 1–12 (1956).

50. Schneider, a S. & Harmatz, D. An experimental method correcting for absorption flattening and scattering in suspensions of absorbing particles: circular dichroism and absorption spectra of hemoglobin in situ in red blood cells. *Biochemistry* **15,** 4158–4162 (1976).

51. Friebel, M., Helfmann, J., Netz, U. & Meinke, M. Influence of oxygen saturation on the optical scattering properties of human red blood cells in the spectral range 250 to 2,000 nm. *J. Biomed. Opt.* **14,** 34001 (2015).

52. Steinke, J. M. & Shepherd, A. P. Diffusion model of the optical absorbance of whole blood. *J. Opt. Soc. Am. A.* **5,** 813–22 (1988).

53. Grewe, M. G., Gururaja, T. R., Newnham, R. E. & Shrout, T. R. Acoustic Properties of Article/Polymer Composites for Transducer Backing Applications. *Ultrason. Symp.* **37,** 713–716 (1989).

54. Wang, H., Cao, W. & Shung, K. High Frequency Properties of Passisve Material for Ultrasonic Transducer.pdf. *IEEE Trans Ultrason Ferroelectr Freq Control* **48,** 78–84 (2001).

55. Azhari, H. Appendix A - Typical acoustic properties of tissues. *Basics Biomed. Ultrasound Eng.* 313–314 (2010). doi:10.1002/9780470561478

56. Gómez Alvarez-Arenas, T. E. Acoustic impedance matching of piezoelectric transducers to the air. *IEEE Trans. Ultrason. Ferroelectr. Freq. Control* **51,** 624–633 (2004).

57. Honda, Y. & Fitzgerald, P. J. Frontiers in intravascular imaging technologies. *Circulation* **117,** 2024–2037 (2008).

58. Rathod, K. S., Hamshere, S. M., Jones, D. A. & Mathur, A. Intravascular Ultrasound Versus Optical Coherence Tomography for Coronary Artery Imaging – Apples and Oranges? *Interv. Cardiol. Rev.* **10,** 8 (2015).

59. Zacharatos, H., Hassan, A. E. & Qureshi, A. I. Intravascular Ultrasound: Principles and Cerebrovascular Applications. *Am. J. Neuroradiol.* **31,** (2010).

60. ten Hoff, H. *et al.* Mechanical scanning in intravascular ultrasound imaging: artifacts and driving mechanisms: *Eur. J. Ultrasound* **2,** 227–237 (1995).

61. Orford, J. L. *et al.* Frequency and correlates of coronary stent thrombosis in the modern era: Analysis of a single center registry. *J. Am. Coll. Cardiol.* **40,** 1567–1572 (2002).

62. Ong, A. T. L. *et al.* Thirty-day incidence and six-month clinical outcome of thrombotic stent occlusion after bare-metal, sirolimus, or paclitaxel stent implantation. *J. Am. Coll. Cardiol.* **45,** 947–953 (2005).

63. Moussa, I. *et al.* Subacute stent thrombosis in the era of intravascular

ultrasound-guided coronary stenting without anticoagulant: Frequency, predictors and clinical outcome. *J. Am. Coll. Cardiol.* **29,** 6–12 (1997).

64. Madder, R. D., Steinberg, D. H. & Anderson, R. D. Multimodality direct coronary imaging with combined near-infrared spectroscopy and intravascular ultrasound: Initial US experience. *Catheter. Cardiovasc. Interv.* **81,** 551–557 (2013).

65. Jansen, K., Wu, M., van der Steen, A. F. W. & van Soest, G. Photoacoustic imaging of human coronary atherosclerosis in two spectral bands. *Photoacoustics* **2,** 12–20 (2014).

66. Abran, M. *et al.* Validating a bimodal intravascular ultrasound (IVUS) and near-infrared fluorescence (NIRF) catheter for atherosclerotic plaque detection in rabbits. *Biomed. Opt. Express* **6,** 3989 (2015).

67. Thukkani, A. K. & Jaffer, F. a. Intravascular near-infrared fluorescence molecular imaging of atherosclerosis. *Am. J. Nucl. Med. Mol. Imaging* **3,** 217–31 (2013).

68. Bozhko, D. *et al.* Quantitative intravascular biological fluorescence-ultrasound imaging of coronary and peripheral arteries *in vivo. Eur. Hear. J. – Cardiovasc. Imaging* jew222 (2016). doi:10.1093/ehjci/jew222

69. Aikawa, E. *et al.* Multimodality Molecular Imaging Identifies Proteolytic and Osteogenic Activities in Early Aortic Valve Disease. *Circulation* **115,** 377–386 (2007).

70. Chen, J. *et al.* In vivo imaging of proteolytic activity in atherosclerosis. *Circulation* **105,** 2766–71 (2002).

71. Khamis, R. Y. *et al.* Near Infrared Fluorescence (NIRF) Molecular Imaging of Oxidized LDL with an Autoantibody in Experimental Atherosclerosis. *Sci. Rep.* **6,** 21785 (2016).

72. Calfon, M. A. *et al.* In vivo Near Infrared Fluorescence (NIRF) Intravascular Molecular Imaging of Inflammatory Plaque, a Multimodal Approach to Imaging of Atherosclerosis. *J. Vis. Exp.* 1–5 (2011). doi:10.3791/2257

73. Fox, I., Brooker, L., Heseltine, D., Essex, H. & Wood, E. New dyes for continuous recording of dilution curves in whole blood independent of variations in blood oxygen saturation. in *American Journal of Physiology* **187,** 599 (1956).

74. Caesar J, Shaldon S, et al. The use of indocyanine green in the measurement of hepatic blood flow and as a test of hepatic function. *Clin. Sci.* **21,** 43–57 (1961).

75. Desmettre, T., Devoisselle, J. M. & Mordon, S. [Fluorescence properties and metabolic features of fluorescein]. *J. Fr. Ophtalmol.* **23,** 821–34

(2000).

76. Vinegoni, C. *et al.* Indocyanine Green Enables Near-Infrared Fluorescence Imaging of Lipid-Rich, Inflamed Atherosclerotic Plaques. *Sci. Transl. Med.* **3,** 84ra45-84ra45 (2011).

77. Landsman, M. L., Kwant, G., Mook, G. a & Zijlstra, W. G. Light-absorbing properties, stability, and spectral stabilization of indocyanine green. *J. Appl. Physiol.* **40,** 575–583 (1976).

78. Newman, P. J. *et al.* PECAM-1 (CD31) cloning and relation to adhesion molecules of the immunoglobulin gene superfamily. *Science (80-.).* **247,** 1219–22 (1990).

79. Xie, Y. & Muller, W. A. Fluorescence in situ hybridization mapping of the mouse platelet endothelial cell adhesion molecule-1 (PECAM1) to mouse chromosome 6, region F3-G1. *Genomics* **37,** 226–228 (1996).

80. Inoue, T. *et al.* Vascular Inflammation and Repair. *JACC Cardiovasc. Interv.* **4,** 1057–1066 (2011).

81. Lee, S. *et al.* Fully integrated high-speed intravascular optical coherence tomography/near-infrared fluorescence structural/molecular imaging in vivo using a clinically available near-infrared fluorescence-emitting indocyanine green to detect inflamed lipid-rich atherom. *Circ. Cardiovasc. Interv.* **7,** 560–569 (2014).

82. Bozhko, D., Gorpas, D., Jaffer, F. A. & Ntziachristos, V. Intravascular optoacoustic catheter with extended sensitivity field. in *Progress in Biomedical Optics and Imaging - Proceedings of SPIE* **10415,** (2017).

83. Bourantas, C. V. *et al.* Hybrid intravascular imaging: recent advances, technical considerations, and current applications in the study of plaque pathophysiology. *Eur. Heart J.* ehw097 (2016). doi:10.1093/eurheartj/ehw097

84. Ughi, G. J. *et al.* Dual modality intravascular optical coherence tomography (OCT) and near-infrared fluorescence (NIRF) imaging: a fully automated algorithm for the distance-calibration of NIRF signal intensity for quantitative molecular imaging. *Int. J. Cardiovasc. Imaging* **31,** 259–268 (2015).

85. Abran, M. *et al.* Development of a photoacoustic, ultrasound and fluorescence imaging catheter for the study of atherosclerotic plaque. *IEEE Trans. Biomed. Circuits Syst.* **8,** 696–703 (2014).

86. Yoneya, S. *et al.* Binding properties of indocyanine green in human blood. *Invest. Ophthalmol. Vis. Sci.* **39,** 1286–1290 (1998).

87. Jaffer, F. A. *et al.* Real-time catheter molecular sensing of inflammation in proteolytically active atherosclerosis. *Circulation* **118,** 1802–1809 (2008).

88. Esenaliev, R. O., Petrov, Y. Y., Hartrumpf, O., Deyo, D. J. & Prough, D. S. Continuous, noninvasive monitoring of total hemoglobin concentration by an optoacoustic technique. *Appl. Opt.* **43,** 3401 (2004).

89. Esenaliev, R. O. *et al.* Optoacoustic technique for noninvasive monitoring of blood oxygenation: a feasibility study. *Appl. Opt.* **41,** 4722 (2002).

90. Phinikaridou, A., Hallock, K. J., Qiao, Y. & Hamilton, J. A. A robust rabbit model of human atherosclerosis and atherothrombosis. *J. Lipid Res.* **50,** 787–797 (2009).

91. Sukhova, G. K., Shi, G. P., Simon, D. I., Chapman, H. A. & Libby, P. Expression of the elastolytic cathepsins S and K in human atheroma and regulation of their production in smooth muscle cells. *J. Clin. Invest.* **102,** 576–83 (1998).

92. Liu, J. *et al.* Lysosomal cysteine proteases in atherosclerosis. *Arterioscler. Thromb. Vasc. Biol.* **24,** 1359–66 (2004).

93. Jaffer, F. A. *et al.* In vivo imaging of protease activity in atherosclerosis using a near-infrared fluorescence intravascular catheter. *Circulation* **114,** 414 (2006).

94. Hara, T. *et al.* Molecular imaging of fibrin deposition in deep vein thrombosis using fibrin-targeted near-infrared fluorescence. *JACC Cardiovasc. Imaging* **5,** 607–615 (2012).

95. Bruining, N. *et al.* ECG-gated versus nongated three-dimensional intracoronary ultrasound analysis: Implications for volumetric measurements. *Cathet. Cardiovasc. Diagn.* **43,** 254–261 (1998).

96. von Birgelen, C. *et al.* ECG-Gated Three-dimensional Intravascular Ultrasound : Feasibility and Reproducibility of the Automated Analysis of Coronary Lumen and Atherosclerotic Plaque Dimensions in Humans. *Circulation* **96,** 2944–2952 (1997).

97. Roelandt, J. R. *et al.* Three-dimensional reconstruction of intracoronary ultrasound images. Rationale, approaches, problems, and directions. *Circulation* **90,** 1044–1055 (1994).

98. Di Mario, C. *et al.* Three dimensional reconstruction of cross sectional intracoronary ultrasound: clinical or research tool? *Br. Heart J.* **73,** 26–32 (1995).

99. Rosales, M., Radeva, P., Rodriguez-Leor, O. & Gil, D. Modelling of image-catheter motion for 3-D IVUS. *Med. Image Anal.* **13,** 91–104 (2009).

100. Jansen, K., van der Steen, A. F. W., van Beusekom, H. M. M., Oosterhuis, J. W. & van Soest, G. Intravascular photoacoustic imaging of human coronary atherosclerosis. *Opt. Lett.* **36,** 597–9 (2011).

101. Joner, M. *et al.* Pathology of Drug-Eluting Stents in Humans. Delayed Healing and Late Thrombotic Risk. *J. Am. Coll. Cardiol.* **48,** 193–202 (2006).

102. Finn, A. *et al.* Pathological correlates of late drug-eluting stent thrombosis: Strut coverage as a marker of endothelialization. *Circulation* **115,** 2435–2441 (2007).

103. Mauri, L. *et al.* Twelve or 30 months of dual antiplatelet therapy after drug-eluting stents. *N. Engl. J. Med.* **371,** 2155–66 (2014).

104. Choi, S. Y. *et al.* Intravascular ultrasound findings of early stent thrombosis after primary percutaneous intervention in acute myocardial infarction: A harmonizing outcomes with revascularization and stents in acute myocardial infarction (HORIZONS-AMI) substudy. *Circ. Cardiovasc. Interv.* **4,** 239–247 (2011).

105. Cao, Y. *et al.* High-sensitivity intravascular photoacoustic imaging of lipid–laden plaque with a collinear catheter design. *Sci. Rep.* **6,** 25236 (2016).

9 Funding.

10 Acknowledgements.

11 Appendix.

Erklärung

Ich versichere hiermit, dass ich die von mir eingereichte Abschlussarbeit selbstständig verfasst und keine anderen als die angegebenen Quellen und Hilfsmittel benutzt habe.

Ort, Datum, Unterschrift